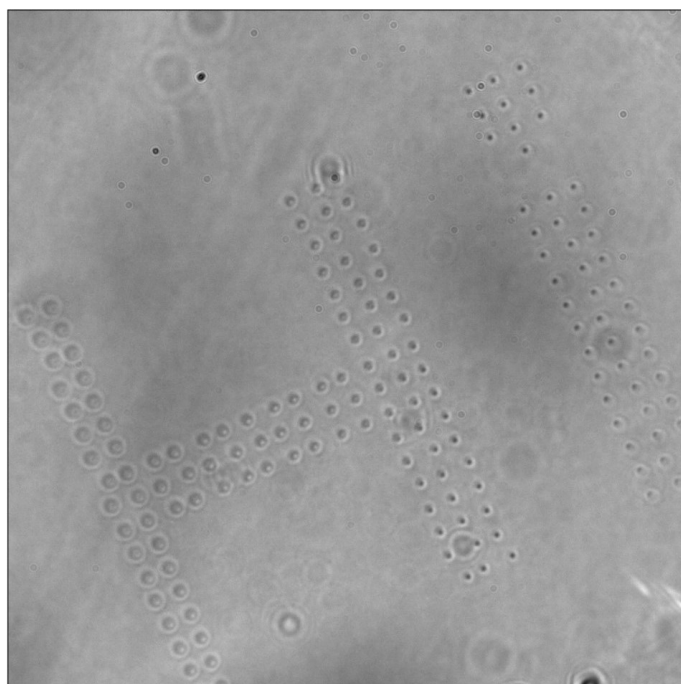




Utrecht University



Master's thesis

Lensless imaging and laser engraving in 3D

Dennis Kooijman B.Sc.

First examiner:

Prof. Dr. Allard P. Mosk

Second examiner:

Dr. Dries van Oosten

Daily supervisor:

Jacob Seifert, M.Sc.

Nanophotonics research group

Debye Institute for Nanomaterials Science

Faculty of Science

Utrecht University

Nanomaterials Science Tuesday 31st January, 2023

Abstract

In this work, the idea was to improve the automatic differentiation framework 'Ptychoflow', allowing the reconstruction of 3D objects. To create test objects, we have used sub-surface laser engraving on BK-7 glass, resulting in multidimensional objects. The advantage of these objects lies in the prior information one would know regarding the objects. By using Ptychoflow, we have shown that our objects, created through sub-surface laser engraving, contain both amplitude and phase information. Utilising this information, combined with numerical data, we have shown that Ptychoflow is now capable of reconstructing 3D objects.

Contents

1	Introduction	5
2	Theory	7
2.1	Sub-surface laser engraving to create multidimensional objects	7
2.1.1	BK-7 glass for sub-surface laser engraving	7
2.1.2	Nature of femtosecond pulses and interaction with materials .	7
2.1.3	Non-linear effects for high intensities	8
2.1.4	Filament propagation	9
2.1.5	Avalanche ionization alter refractive index for femtosecond pulse duration	10
2.2	Ptychography	10
2.2.1	Automatic differentiation algorithm	11
2.2.2	Angular spectrum method	13
2.2.3	Multi-slice ptychography	14
2.2.4	Multi-slice reconstruction by automated differentiation ptychography	15
2.3	Evaluating reconstruction quality by complex correlation	16
3	Methods	17
3.1	BK-7 glass sample preparation	17
3.2	Sub-surface laser engraving to create samples for 2 and 3D reconstruction	17
3.2.1	2 and 3D model to a list of coordinates	17
3.2.2	Sub-surface laser engraving through laser setup	18
3.2.3	Bright-field transmission microscope	20
3.3	Automatic differentiation ptychography	20
3.3.1	Ptychography setup	20
3.3.2	Experimental reconstruction of experimental diffraction patterns using AD-based algorithm	22
3.4	Simulating data and analysing	23
3.4.1	3D object consisting of two 2D independent layers	23
3.4.2	Fermat spiral to create scanning points	24
3.4.3	Flat probe as illumination source	25
3.4.4	Simulating diffraction patterns and reconstructing the 3D object	25
4	Results and discussion	27
4.1	Determining the laser parameters	27
4.1.1	Determining damage threshold and visualizing damage in BK-7 glass in X,Y dimensions using a single pulse	27
4.1.2	Influence of multiple pulses for the size in XY dimension of BK-7 glass	28
4.2	Sub-surface laser engraving for 2D ptychography	30
4.2.1	Validating software to perform sub-surface laser engraving . .	30
4.2.2	2D Ptychography measurement and reconstruction	31
4.2.3	3D ptychography measurement and reconstruction	33
4.3	3D object reconstructed based on numerical data	37
5	Conclusion	41

References	42
A Creating numerical data	45

1 Introduction

Imaging the region of interest has been and will be an important aspect of daily life, as the human eye is the oldest imaging device. Imaging allows visualising a sample, even if the resolution is far beyond what the human eye can witness. Therefore, it is used in a wide range of fields and techniques such as biophysics[1], electron microscopy [2] and molecular imaging [3]. Imaging is so important in science, it is a multidisciplinary field which takes interest in the generation, gathering, repeatability, analysis, alterations and showing of images [4]. Imaging science has many subfields for which research is performed, such as astronomical, holography, radar and chemical imaging. However, since the rapid improvement of the current technology, computational imaging is improving rapidly.

Computational imaging combines the joint design of front-end optics with post-detection signal processing. It is the process, in which the sample is reconstructed using an algorithm based on measurements by using sufficient computational resources. Therefore, the data captured from a sample might not even seem like an image. For computational imaging, a design can be created for a setup, capable of taking optical measurements. Then, through the acquired data, the sample and other information can be derived with a capacity exceeding that of physical optics. Furthermore, the field allows designing instruments which have reduced size, weight, power and or cost versus conventional approaches [5]. There are many applications in which computational imaging is used, for example in computed tomography and magnetic resonance imaging.

Another computational imaging technique is ptychography. The term 'Ptychography' was originally used by Hoppe in 1969 [6]. It was thought to act as a solution for the electron crystallographic phase problem. However, the phase problem could not be solved for crystals due to their nature. However, 20 years later, an iterative phase retrieval method was proposed which utilizes diffraction patterns. These diffraction patterns were measured in intensity, which allows for solving both the amplitude and phase of an image wave function. Hereby, in comparison to the original concept envisioned by Hoppe, it is able to take non-crystalline objects into consideration [7]. Ptychography does not depend on the need for a lens. Therefore, the resolution limiting factor is the angle at which the detector will detect the scattering. The technique is therefore ideal to be used in X-ray [8], extreme ultraviolet [9] or electron ptychography [10] as those often require special lenses or there are no suitable lenses in the wavelength regime available.

Since the re-introduction of ptychography, the number of fields in which it is used keeps increasing, therefore sub-categories of ptychography are emerging. One of these is automated diffraction ptychography (ADP) [11]. In the last few years, it has been shown that through optimizing based on automatic differentiation, the inverse problem can be solved [12][13]. Therefore, ADP will not depend on an analytical derivation regarding the update function. Furthermore, the rapidly increasing progress regarding machine learning allows an improvement for ADP in the form of hardware, algorithms, and software.

This thesis will use automated-differentiation ptychography (ADP) to reconstruct a 3D object. This 3D object will be created by using sub-surface laser engraving. Therefore, this thesis consists of two main parts. In the first part, sub-surface laser engraving will be optimized for the creation of 2 and 3D objects in BK-7 glass. By using sub-surface laser engraving, we will have control and prior information regarding the 3D object. Then, in the second part, we will validate the extension

allowing 3D objects to be reconstructed through experimental and numerical data. The experimental data will be captured by using the created 2 and 3D sub-surface laser engraved objects, while a simulation will be used to create numerical data of a 3D object. Then, both experimental and numerical data will be reconstructed to verify the extension to 3D. The application of 3D lensless imaging could be found in the areas in which a lens would limit the resolution. For example, in X-ray research or in the process of developing semiconductors by visualising the individual layers to inspect them, in which reaching a resolution of nanometres is desirable.

The main advantages of ptychography can be summarized in 4 points. The first point, as mentioned earlier, a setup does not depend on the use of lenses. Hence, ptychography is able to surpass the resolution of lens-based imaging techniques. In the second point, ptychography is able to simultaneously recover the object and the probe beam by utilizing the captured diffraction patterns. Third, compared to coherent diffraction imaging, there is no need for an isolated object. This difference occurs as the spatially confined probe removes the need for a support constraint in the reconstruction process, as the probe naturally imposes a constraint. Last, the reconstruction is capable of self-calibration, thereby allowing errors in the experimental setup to be corrected for [14].

2 Theory

2.1 Sub-surface laser engraving to create multidimensional objects

2.1.1 BK-7 glass for sub-surface laser engraving

The idea of using a laser to create images was first mentioned in 1970 [15]. Then the company TYKMA Electrox developed and manufactured a commercial laser that allowed laser engraving. However, with the technology regarding computers evolving rapidly, most progress was made in the 90 and begin 2000s. At that time, only 2D objects were possible to be engraved. However, Troitski [16] introduced the formation of an object by altering the volume inside the glass, therefore, creating a 3D object inside the glass. The techniques and software were then optimized, leading to higher resolution 3D objects to be formed[17].

Recently, the durability of the refractive index change induced by a single femtosecond laser pulse in BK-7 glass was studied extensively [18]. Direct laser writing using a 150 fs with 1 KHz repetition rate laser pulse by a Kerr mode-locked and regenerative amplified Ti:Sapphire laser system was performed. The glass was processed in the form of a matrix, with all rows being inscribed by an identical pulse. The energy was increased for each row, ranging from 0.41 to 3.40 μm in 6 rows. By using a phase microscope, the ablation sites could be analysed. The ablation site sizes in the x-y plane ranged from 1 to 3 μm , while the size in the y-z plane was ranging from 20 to 40 μm . Thus, the damage threshold for a 150 femtosecond pulse in BK-7 glass is close to 0.41 μJ . Regarding the material to be used for sub-surface laser engraving, there are two character traits a material has to meet to be suitable for sub-surface laser engraving. The first criterion, for a material, is that the material to be transparent. Second, the material has to remain stable while being damaged to create ablation sites. The first criterion has to be met in order to detect a change in refractive index and be able to create an object anywhere in the material. Therefore, the second criterion has to be met as well, as the material would be unserviceable to laser engraving if it would be shattered in the progress. As BK-7 Glass has been shown as a suitable material for sub-surface laser ablation, it is hypothesized it should be possible to order the ablation sites accordingly in BK-7. By ordering the ablation sites, a structure can be created leading to a sub-surface laser engraved object. In this work, BK-7 glass will be used to ensure a material capable of being transparent and stable is used.

2.1.2 Nature of femtosecond pulses and interaction with materials

The moment a pulse with a femtosecond duration interacts with a material, the material is exposed to a high peak intensity I . This peak intensity I , is the ratio between the applied laser power P and the focused spot size, given by a radius of w_0 . The response of material for femtosecond pulses is nonlinear and different compared to lower-intensity pulses. As the laser travels through a dielectric material, the material will be polarized. In the case of an electric field, caused by a femtosecond pulse, the interaction is non-linear described by equation 1 [[19]].

$$P(t)^4 = \xi_0 X^1 E(t) + \xi_0 X^2 E^2(t) + \xi_0 X^3 E^3(t) + \xi_0 X^4 E^4(t) + \dots \quad (1)$$

For both equations, X^1 is the linear optical sensitivity, with X^N ($N > 1$) being

the Nth order nonlinear optical sensitivity while ξ_0 is the vacuum dielectric permeability. During light interaction, multiple non-linear processes can be induced simultaneously [19]. Therefore, for non-central symmetric materials either the Kerr effect potentially changes propagation conditions if a high I is used or a second-order interaction has to be taken into account [20]. A non-linear response is desired, as only damage in the focus spot is needed. A linear response would result in the creation of additional damage in the glass, away from the focus spot.

2.1.3 Non-linear effects for high intensities

One of the aforementioned non-linear processes is multi-photon absorption. This process occurs when at least two photons are simultaneously excited from the ground to an excited state. Depending on the number of photons (N) simultaneously excited, the absorption is decided by the Nth-order nonlinear optical sensitivity. Thus, higher-order absorption is determined by higher-order of nonlinear optical sensitivity. This absorption can be used in techniques of microscopy and transparent laser processing for a positive effect.

Thus, to create a change in a dielectric material, the electrons within the material have to be excited from the ground state. The three most common and important ones are tunnelling ionization, avalanche ionization, and multiphoton ionization for femtosecond pulses. Tunnelling ionization is caused by laser radiation distorting the barrier containing the electrons, as seen in figure 1c. Multiphoton ionization occurs when an electron absorbs multiple photons and will then be excited through virtual levels, as seen in 1b.

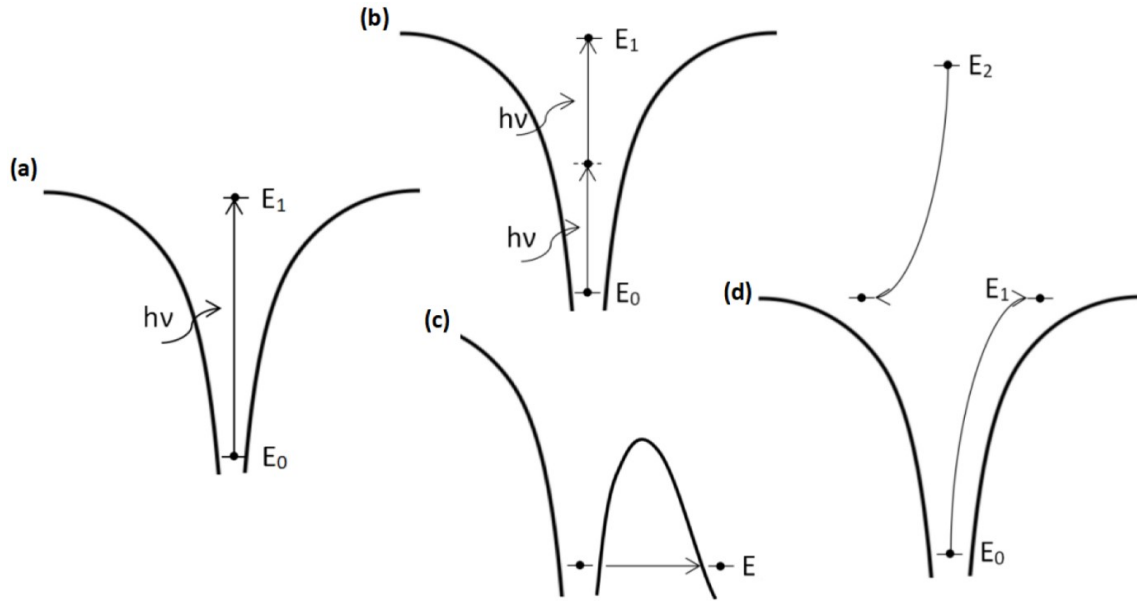


Figure 1: Adopted from [19]. General schemes for different ionization processes. (a) illustrates linear ionization, (b) multiphoton ionization, (c) tunnelling ionization and (d) avalanche ionization

Between multiphoton and tunnelling ionization, it will depend on the intensity and waist of the laser. The dependency can be described by the Keldish parameter in the form of equation [21]:

$$\gamma = \frac{w}{e} \sqrt{\frac{m_e \delta E \xi_0}{I}} \quad (2)$$

In the equation, w is the beam waist, e is the electron charge, m is the electron mass, c is the speed of light, ξ_0 is the vacuum dielectric penetration to the barrier and δE is the reserve strip spacing. In the case, the Keldish parameter is less than 1.5, the tunnelling ionization will dominate and if more, the multiphoton ionization. If the parameter were to be close enough to 1.5 then both contribute equally to the material ionization.

The third process caused by nonlinear radiation is avalanche ionization. The radiation of the laser will interact with the electron, causing them to eject out of its natural state. Then, these electrons are accelerated due to the radiation and their release of the corresponding energy could be enough to eject other electrons [19]. This will cause an avalanche in which more electrons keep being ejected, ultimately reaching the threshold of the material, resulting in permanent changes to the material [20]. These changes include a change in the refractive index, which is desired for sub-surface laser engraving to form controlled structures.

2.1.4 Filament propagation

During laser engraving, filament propagation might occur. This means that the laser beam propagates through the BK-7 glass without diverging. Hereby, the Kerr effect will play a role. There are two forms of the Kerr effect. The first is the Kerr electro-optic effect, commonly known as the DC Kerr effect. However, this effect can be noticed if an external field is applied to the sample. The second form is the optical Kerr effect. This can occur due to the high-power laser causing an electric field which starts to interact with the light itself. Thereby, the Kerr effect is able to cause a change in the refractive index of the BK-7. As no external electric field will be applied in this work, all further referring to the Kerr effect will be the optical Kerr effect.

As mentioned, the refractive index can be changed by the Kerr effect. The refractive index can be described as seen in the equation:

$$n = n_0 + n_2 I \quad (3)$$

Here, n_0 is the linear refractive index, n_2 is the nonlinear refraction coefficient and I is the intensity of the laser beam inside the sample [22].

Based on equation 3, the refractive index will increase for areas with a higher intensity. The ability of the laser to self-focus will start to perform if the phase shift induced by the Kerr effect is able to compensate for the Gaussian beam divergence phase shift. The phase change of a Gaussian beam after moving distance δZ is described by the equation [23]:

$$\phi_{dif} = k \delta z r^2 / 2 \rho_0^2 \quad (4)$$

he phase change due to the Kerr effect is described in equation [23]:

$$\phi_{Kerr} = (2\pi n_2 I_0 \delta z / \lambda) e^{-2r^2/w_0^2} \quad (5)$$

Here, $k = 2\pi n_0 / \lambda$, $p(0)$ is the Rayleigh range and w_0 is the waist of the Gaussian beam. Therefore, in order for self-focussing of to occur, the r^2 terms should be in the same magnitude. By implying the term r^2 are of the same magnitude will result in [23]:

$$I_0 = w_0^2 / 4 p_0^2 n_2 \quad (6)$$

Then by combining equation 6 and the beam waist, a formula for the critical power can be determined [23]:

$$P_c = \lambda^2 / 8\pi n_0 n_2 \quad (7)$$

From this critical power onwards, self-focusing starts to occur [23]. As it is desired to create a refractive index change, a pulse with sufficient intensity will be required. As described, a femtosecond pulse should be capable to induce a refractive index change.

2.1.5 Avalanche ionization alter refractive index for femtosecond pulse duration

The refractive index of a transparent material can be altered locally, for either the surface or sub-surface. In the range of nano- and femtoseconds laser pulse, the laser has to be focussed locally. By focusing the laser locally, the present defects allow the transparent material to absorb the energy. When enough energy is absorbed, the damage threshold can be reached, inducing the breakdown phenomena. Hereby, in the case of femtosecond pulses, the laser-induced breakdown (LIB) will partake through multiple stages [24]:

1. Creation of an initial low-density free electron concentration.
2. Build-up of this electron concentration until the required density is reached.
3. Absorption of the remainder of the laser pulse by the resulting plasma.
4. An increase in temperature to a value of several thousands of degrees.
5. The generation of an initial thermally-induced Sound wave which is the response of the medium following the thermal expansion of the central region during the laser heating pulse, which the sound wave propagates outward.
6. The expansion of created liquid at a rate much slower than the speed of sound.
7. The generation of a pressure-induced sound wave as the liquid forms higher pressure with gradients of the order of several GPA/ μm .
8. The formation of cracks at the liquid/solid interface (Velocities in the range of 1 to 2 km/s).

In the end, through the formation of cracks, the local refractive index can be altered. The refractive index change will depend on the used energy.

2.2 Ptychography

Ptychography is a computational imaging method. The basic principle of a measurement can be explained by a schematic, as seen in figure 2.

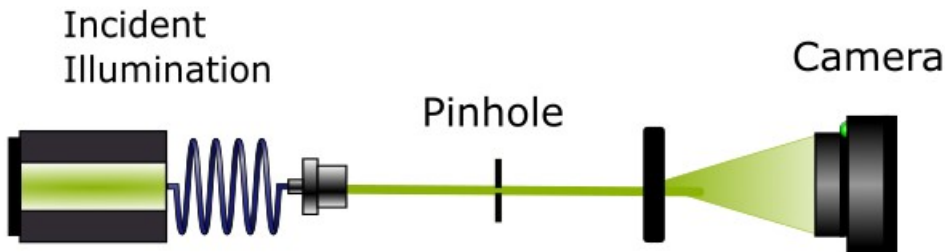


Figure 2: A generic ptychography. A laser is focused on a sample, creating a diffraction pattern. By moving the sample, overlapping diffraction patterns can be created.

Here, a laser is guided through a pinhole to focus on the sample, resulting in a diffraction pattern. The detector then captures the diffraction pattern. By moving the sample, overlapping diffraction patterns can be created and captured. Then, by an algorithm, it is able to solve the inverse problem by using the diffraction patterns, resulting in an image of the sample[14].

The main advantages of ptychography can be summarized in 4 points. The first point, as mentioned earlier, a setup does not depend on the use of lenses. Hence, ptychography is able to surpass the Abbe limit commonly associated with lens-based imaging. In the second point, ptychography is able to simultaneously recover the object and the probe beam by utilizing the captured diffraction patterns. Third, compared to coherent diffraction imaging, there is no need for an isolated object. This difference occurs as the spatially confined probe removes the need for a support constraint in the reconstruction process, as the probe naturally imposes a constraint. Last, the reconstruction is capable of self-calibration, thereby allowing errors in the experimental setup to be corrected for [14].

The influence regarding the overlap of the diffraction pattern has been described by extensively by Bunk[25]. Here, numerical and experimental results on the optimal overlap between different illuminations, taking both the image quality and dose used on the sample in consideration. Simulations have the advantage that the solution is known as the real solution and can be used in combination with an error metric to define the deviations, which takes both amplitude and phase into account. The term 'overlap' is defined as the offset in the linear distance, rather than the areal overlap. Therefore, 2 circles with radius r the absolute overlap can be described by $\gamma = 2r - a$. In which γ is the absolute overlap. Normalizing for the diameter of the circle, the overlap can be described by $\gamma = 1 - a/2r$. The advantage of this definition of overlap, the overlap is a direct parameter to be given for scanning over the positions. The optimal overlap to get the best results depends on a few factors like speed & quality. However, a few important conclusions can be drawn from past research. A general rule of thumb in case of determining the required overlap.

1. The optimum quality of the image is reached using an overlap of 85%. Using a higher overlap will result in an increase in the relative error.
2. A relative overlap of minimally 50% in combination with 5 iterations, the image quality is already acceptable.
3. A relative error of 10^{-2} for an overlap of 60% was found, which was considered an excellent value.

2.2.1 Automatic differentiation algorithm

Recently, a new automated differentiation reconstruction framework was proposed [26]. This framework utilizes TensorFlow and Keras to allow reconstruction and machine learning. For the framework mentioned, the authors compared the proposed AD-based reconstruction to the traditional ptychographical iterative engine (PIE) [27]. There is an essential difference between ptychography iterative engines (PIE) and automatic differentiation (AD). The PIE algorithm uses an iterative update function, whereas, in the new framework, automatic differentiation is used to minimize the loss function [28]. The use of Keras allows a layer-by-layer approach, enabling the reconstruction of the object, similar to the structure of deep neural networks. Hence, the proposed framework compared to PIE will be more adaptable and allow the implementation of changes to the existing or new functions. In the

end, the reconstruction quality and speed were comparable to PIE. However, the proposed framework has not been able to reconstruct 3D objects, even though some other variants of ptychography have been able to.

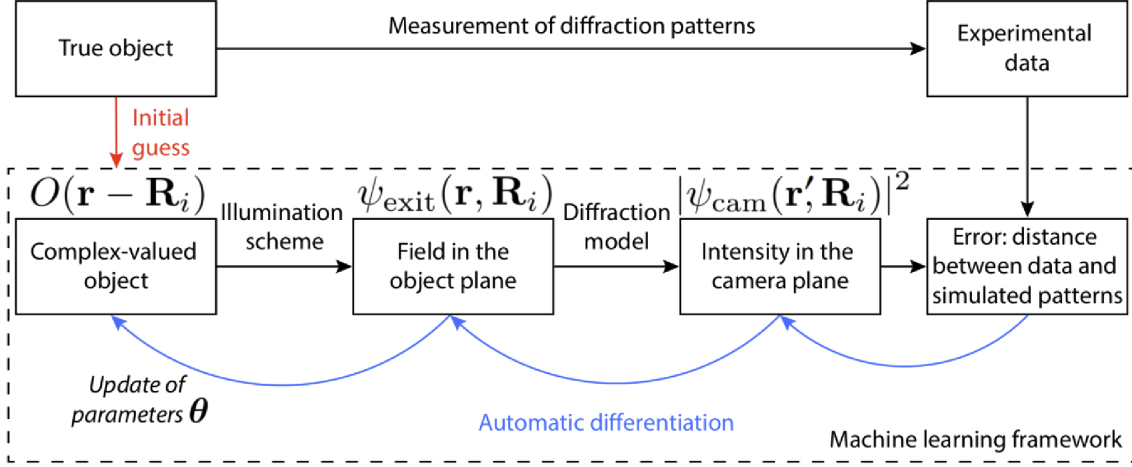


Figure 3: Adopted from [26]. The workflow of the optimization framework for automatic differentiation. Here, the forward model in ptychography is represented by the arrow moving rightwards. The automatic differentiation minimizes the error function by following the grading and updating the object and probe values accordingly.

The automatic diffraction framework used for reconstruction can be seen in figure 3. Overall, the arrows moving to the right indicate the forward model and the blue arrows the automatic differentiation. Here, $O(\mathbf{r})$ represents an n -dimensional complex-valued object. $P(\mathbf{r})$ is representing the probe, which has \mathbf{r} being the coordinate vector in the object plane. By illuminating the object at different positions, the probed areas will show a certain overlap depending on the scanning positions. Hence, the object plane $\psi_{\text{exit}}(\mathbf{r}, \mathbf{R}_i)$ is given by $\psi_{\text{exit}}(\mathbf{r}, \mathbf{R}_i) = O(\mathbf{r} - \mathbf{R}_i) \cdot P(\mathbf{r})$.

The field in the object plane described by $\psi_{\text{exit}}(\mathbf{r}, \mathbf{R}_i)$ can then be modulated by using an appropriate diffraction model. Both the Fresnel diffraction model and the angular spectrum method could be used. The choice for the diffraction model will depend on the propagation distance. For near-field, often the Fresnel diffraction is employed, whereas for far-field the Fraunhofer diffraction is chosen. In this work, however, the angular spectrum is used. However, the method requires two Fourier transforms versus the single one needed in the Fresnel diffraction method. Therefore, the angular spectrum method will be more computationally heavy and take more time per iteration. By selecting the diffraction model, the wave field will be modulated for the propagation distance and by squaring the wave field followed by taking the absolute, the intensity in the detection plane can be calculated. In here $I_{\text{pred}}(\mathbf{r}', \mathbf{R}_i, \boldsymbol{\theta})$ is the guessed coherent diffraction pattern at the current iteration given the described model based on parameters $\boldsymbol{\theta}$. $\boldsymbol{\theta}$ can include the amplitude, and phase values of the probe field and the object. For each iteration, the algorithm will try to minimize the error. The error is given by the mean squared error function [29]:

$$\text{MSE} = \frac{1}{N} \sum_{i=1}^N (I_{\text{meas}}(\mathbf{r}', \mathbf{R}_i) - I_{\text{pred}}(\mathbf{r}', \mathbf{R}_i, \boldsymbol{\theta}))^2 \quad (8)$$

Here, N is the total number of scanning points, with $I_{\text{meas}}(\mathbf{r}', \mathbf{R}_i)$ being the experimental diffraction pattern at the corresponding scanning position [26]. The key concept of ADP is to rely on the optimizer to update the parameters accordingly

to minimize the error and thus reconstruct both the probe and object. The rapid improvement in GPU's has allowed computers to sequentially perform functions of operations under the condition, that the derivation of the function is known.

The derivative of the object function will be known by using the chain rule. Hence, the AD-based framework does not need an analytical expression of the update function compared to other algorithms [26].

2.2.2 Angular spectrum method

By using a suitable diffraction model, the field in detection plane ψ_{exit} with the coordinate vector (\mathbf{r}) can be modulated. In the proposed AD-based framework 'Ptychoflow' [26], both the angular spectrum method and the Fraunhofer diffraction model are implemented. However, in this thesis, the calculation will be performed using the angular spectrum method. At the advantage of superior computational speed, the Fraunhofer diffraction model only performs one fast Fourier transform, whereas the angular spectrum method requires two fast Fourier transformers. However, the advantage of the angular spectrum method is the ability to model for both near- and far-field diffraction and thus resulting in a more accurate reconstruction of both the probe and object.

The method functions by expanding a complex wave field of a sum of infinite plane waves of the same frequency but in different directions for the monochromatic disturbance. Then, by adding the contribution of the Fourier-analysed and taking the phase shift of the plane waves into account, the field amplitude can be calculated.

To derive the formula for the angular spectrum method, several steps are needed. The first step is to consider a wave illuminating on a transverse (x,y) plane, which propagates in the Z-direction. The complex field at the $Z = 0$ plane can be described by $U(x,y,0)$. This situation can be used to calculate the resulting field at a certain position Z within U , which is a parallel plane at a point Z compared to $z = 0$. At $z = 0$, the two-dimensional Fourier transform of U is then given by [30]:

$$A(f_x, f_y, 0) = \int_{-\infty}^{\infty} U(x, y, 0) e^{-j2\pi(f_x x + f_y y)} dx dy \quad (9)$$

This means that in the case of a plane at $Z = 0$, the complex-exponential part of the equation can be seen as a representation of a plane wave propagating with [30]:

$$\begin{aligned} \alpha &= \lambda f_x \\ \beta &= \lambda f_y \\ \gamma &= \sqrt{1 - (\lambda f_x)^2 - (\lambda f_y)^2} \end{aligned}$$

This means that the complex amplitude of the plane wave component, which contains spatial frequencies (f_x, f_y) , can be written as $A(f_x, f_y) df_x df_y$. Therefore, the angular spectrum for $U(x,y,0)$ [30]:

$$A(\alpha/\lambda, \beta/\lambda, 0) = \int_{-\infty}^{\infty} U(x, y, 0) e^{-j2\pi(\alpha/\lambda x + \beta/\lambda y)} dx dy \quad (10)$$

By using the angular spectrum at $z = 0$, the angular spectrum at $z = z$ can be described by the following equation [30]:

$$A(x, y, z) = \int_{-\infty}^{\infty} A(F_x, F_y, F_z) e^{j2\pi(F_x x + F_y y)} dx dy \quad (11)$$

Then by introducing a bandwidth limitation which is connected to the evanescent wave by using a circ function [30], the function can be rewritten to:

$$A(f_x, f_y, z) = \int_{-\infty}^{\infty} A(F_x, F_y, 0) \text{circ}(\sqrt{(\lambda f_x)^2 + (\lambda f_y)^2} e(j2\pi z/\lambda \sqrt{1 - (\lambda f_x)^2 - (\lambda f_y)^2})) \quad (12)$$

Which leads to the transfer function of the wave propagation to be [30]:

$$H(f_x, f_y) = e(j2\pi z/\lambda) \sqrt{1 - (\lambda f_x)^2 - (\lambda f_y)^2} \text{if } \sqrt{f_x^2 + f_y^2} < 1/\lambda \quad (13)$$

The equation illustrates that the propagation can be seen as a linear, dispersive spatial filter in the case of a finite bandwidth. Additionally, if the radius exceeds $1/\lambda$, the values will be 0 [30].

Hence, the method can be summarised in four steps:

1. For a pressure field over a grid of points within a cross-sectional plane contained in the field, the complex is sampled in complex components.
2. The 2D Fourier transform of the pressure field is performed. Hereby, the pressure field will be split into 2D angular spectrum plane waves which travel in different directions.
3. A propagation parameter is multiplied with each point in the 2D Fourier transform. The propagation parameter takes the phase change for each individual plane into consideration.
4. By taking the 2D inverse Fourier transform of the individual plane waves multiplied by the propagation parameter, the predicted plane waves will be found.

2.2.3 Multi-slice ptychography

The existing 2D ptychography algorithms with strong robustness to noise due to the redundant data created by the large overlap between probed areas in a measurement. The information within a diffraction pattern contains more than the 2D object and corresponding probe. For example, the partial coherence of the probe, information regarding the third dimension of the object and the sample positions of the scanning points. This resulted in the creation of the multi-slice ptychography algorithm (MSP) [31]. The overlapping scan encodes the difference in depth for different slices at different moving rates, to be detected across the detector plane. Therefore, the correlation between neighboured diffraction patterns allows the ptychography to extract the depth information and utilize this information in reconstructions [31].

In Loetgering et al [32], two independent layers could be reconstructed by the introduction of the auto-focusing zPIE. There were two fingerprints placed on both sides of a 1 mm glass. The fingerprints were placed to create both overlapping and non-overlapping regions and the diffraction patterns were captured, so the reconstruction could be performed. First, by using the zPIE algorithm, the thickness could be retrieved for the glass through a single-slice experiment. Single-slice comparison to multi-slice ptychography showed the single slice to exhibit inferior spatial resolution. The reconstruction of both fingerprints could however be done using single slices.

In 2D ptychography, a sample's thickness is assumed to be negligible. Thereby, the algorithms are not designed to handle multiple scattering effects which can occur within thick samples [33]. The MSP is able to solve this problem without the need to change the experimental setup. In the algorithm, the sample is divided into

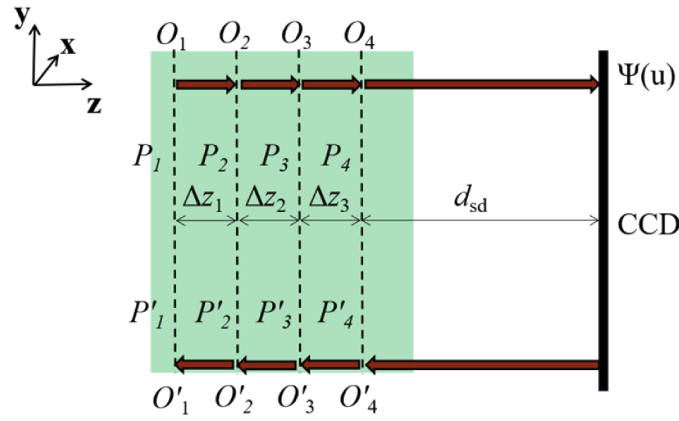


Figure 4: Taken from [35]. In the algorithm, the object is divided into several 2D slices. At each slice, the wave field interacts by multiplying with the slice transmission function to model for the multiple scattering effects, whereas in the vacuum between slices the wave field propagates freely. During the back transmission of the wave field, both the object and probe functions are updated simultaneously.

several slices perpendicular to the optical axis, while each slice is treated as a 2D layer. Therefore, the assumption for 2D ptychography, the thickness of a sample is negligible, can be used. Therefore, the wavefront of the laser source propagates from the nearest slice to the next slice, with which it multiplies. This is repeated till the last slice is reached and from there on the exit field will propagate to the detector plane in the far field. Then, the wave function will be updated on the camera plane. Thereafter, the wavefront will be transmitted back, running through each slice and updated along with each slice. The updating functions can be kept the same as for 2D ptychography[31]. A schematic of multi-slice ptychography can be seen in fig 4. The algorithm has since then been tested for both X-ray [34] and visible light [31].

The MSP, however, has its limitations. These limitations include the small number of slices which can be reconstructed, the redundancy and the needed high overlap of a dataset. This results in the algorithm having trouble, if possible at all, reconstructing the object. This is caused by the algorithm's updating process being started with the object and probe closest to the detector. Therefore, the quality of reconstructions closest to the illumination source will depend on the quality of the reconstruction closest to the detector. This can result in differences between reconstruction quality and or convergence speed [35].

2.2.4 Multi-slice reconstruction by automated differentiation ptychography

As stated in the previous section, the reconstruction for multi-slice ptychography has limitations for the number of slices capable to be reconstructed. By using ADP, these limitations could be avoided as the algorithm functions by automatic differentiation as described in section 2.2.1. However, the AD-based framework by Seifert et al [26], has not been designed for 3D object reconstruction. The implementation reconstructs the 2D layer as seen in figure 5a. Here, the object will be illuminated by the probe, creating an overlap between the diffraction patterns. Then, the exit field in the 2D layer will be depending on both the probe and the object. The exit field is then modulated to the detector by the angular spectrum method, from which the intensity can be calculated. However, if the exit field would be allowed to modulate to a different independent 2D layer, rather than directly to the detector, an updated

exit field can be calculated. The same process could then be repeated for a new 2D layer or, when there are no more 2D layers, to the detector. There, the intensity could still be calculated and used to calculate the mean squared error. The new implementation can be visualized in 5b. Here, two independent 2D layers are used, but in theory, hundreds of layers could be used. In practice, however, absorption of the light by the layers will at some point reduce the ability of the algorithm to solve the layers and phase. In the implementation, the distance between the layers is a parameter dz .

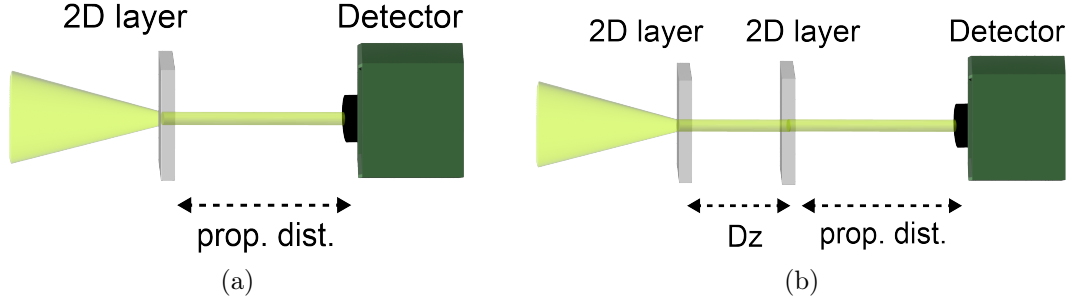


Figure 5: Schematic of the old implementation for reconstructing the object limited to 2D (a) and the new implantation capable of reconstructing 3D objects (b) using a distance between layers, described by dz .

2.3 Evaluating reconstruction quality by complex correlation

To allow a quantitative statement regarding the quality of the reconstruction, an equation capable of comparing the reconstructed complex layer to the known solution. Therefore, the complex correlation function seen in equation 14 can be used.

$$C = \frac{\sum_{i=1}^n O^*(r_i) \hat{O}(r_i)}{\sqrt{\sum_{i=1}^n |O(r_i)|^2} \sqrt{\sum_{i=1}^n |\hat{O}(r_i)|^2}} \quad (14)$$

Here, O_{r_i} is the known solution to the reconstruction, while $\hat{O}(r_i)$ is the reconstructed object. N is the total number of pixels per image. In theory, the reconstructed object could undergo a spacial shift compared to the known solution. This is an ambiguity within all forms of ptychography. This could be countered by estimating the shift and shifting either the known solution or the reconstructed object to the same coordinates. However, the potential shift depends on the probe. If the probe were to be fixed at the centre, the shift will be prevented from occurring. Therefore, it will not be needed to correct the reconstructed object or the known solution to compare to each other. By correlating the reconstructed object and the known solution, the correlation coefficient C can be calculated. This coefficient will then consist of a real and complex part. By taking the absolute value of this coefficient C , the coefficient will give a quantitative indicator for how well the reconstructed object resembles the known solution.

3 Methods

3.1 BK-7 glass sample preparation

A customized BK-7 glass sample was used to perform sub-surface laser engraving and measurements of the diffraction patterns, allowing automatic-differentiation ptychography. The original uncoated BK-7 glass was obtained from Thorlabs, listed as product number WG10530. The sample has a diameter of 12.7 mm with a thickness of 3 mm. The glass from Thorlabs has been modified. Three chrome dots with a diameter of 1 mm were placed on top of the sample through evaporation, at 2 mm from the edge. The dots serve as a reference point for sub-surface laser engraving and ptychography measurements. A photograph of the modified BK-7 glass sample can be seen in figure 6.



Figure 6: Image of the sample (uncoated BK-7 glass) with a diameter of 12.7 mm and a height of 3 mm. The three chrome dots are placed at 2 mm from the edge, with the two dots being 2 mm apart. The chrome dots have a diameter of 1 mm.

3.2 Sub-surface laser engraving to create samples for 2 and 3D reconstruction

3.2.1 2 and 3D model to a list of coordinates

In order to engrave a multidimensional object in the BK-7 glass, the laser engraving setup requires a list of volumetric sampling points resembling the object. Therefore, two scripts were written, capable to translate a 2 or 3D model to a set of coordinates. First, a 2 or 3D object is transformed into a list of volumetric sampling points. Then, a few parameters to this list can be added, these are the pulse energy, distance between volumetric sampling points, and the number of pulses per point. Additionally, the scripts are indirectly able to influence the number of points, although giving in an exact amount of coordinates is not possible currently. However,

Table 1: Table for the parameters used to create the coordinate lists.

Parameters	Exp 1	Exp 2	Exp 3	Exp 4
Shape	'R'	'R'	'T' & 'H'	'T' & 'H'
Pulse strength (SI μ J)	1.1	1.1	1.1	1.1
Total volumetric sampling points	162	3662	8273	6871
Distance between sides (μ m)	5.0	1.0	1.0	1.5
Pulses per coordinate	1	64	64	64

as the number of volumetric sampling points to create a 3D structure could go towards the order of 10^3 or more, adding or losing a single damaged site is neglectable. By combining the distance between coordinates and the number of them, the size of the to be sub-surface laser engraved structure can be tuned. These scripts were used to transform 2 models into a list of coordinates. However, this resulted in 4 lists of coordinates, two for each model in which the parameters for the coordinate list are different. The list of parameters can be seen in table 1 and the coordinate list of Exp 2 and Exp 4 have been plotted. These can be seen in figure 7. Here, it can be confirmed that Exp 2 indeed forms the letter 'R', while Exp 4 recreates the letters 'T' & 'H' at depth difference of $150\mu\text{m}$

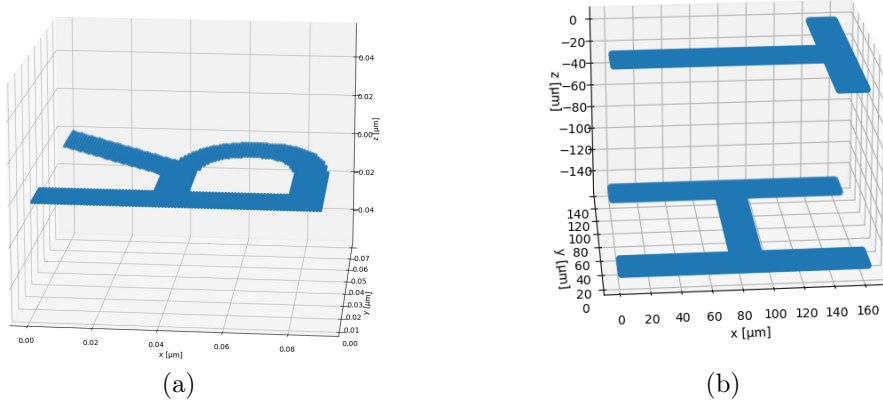


Figure 7: Translated 3D model of the letter 'T' & 'H' combined with the settings seen in table 1, under column Exp 2 (a) and Exp 4(2).

3.2.2 Sub-surface laser engraving through laser setup

To perform a sub-surface laser engraving experiment, a setup designed for ablation experiments will be used. The setup has many features designed for ablation experiments. In this thesis, not all features were used and therefore will not be mentioned. However, if the reader wishes to examine all the details regarding the setup, they are suggested to read the paper regarding the setup by Vreugdenhil et al [36]. Regarding the used features and specifics, the illumination source in the setup is a light conversion pharos PH-2-SP-1-mJ. This laser was operated at a wavelength of 1034nm and a full-width half maximum of 12nm . The setup was used with both single-shot and multi-shot to introduce ablation. In both cases, a pulse duration of 20fs was used. Furthermore, for the multi-shot ablations, a repetition rate of 50kHz was used.

In the setup (figure 8), the light from the laser will be guided through the half-wave plate ($\lambda/2$), which is mounted on a motorized rotation stage. Then, the light will travel past a polarizing beam splitter, allowing automatic scanning of the pulse energy. The neutral density filter (ND) is then able to further tune the pulse energy. The light will then reach two pellicle beam splitters from Thorlabs (BP145B2), placed at an angle of $\pm 45^\circ$ with respect to the direction of the laser propagation. The beam splitters have transmission and reflection coefficients of respectively 0.83 and 0.17, at the used laser wavelength (1034 nm). A small part will therefore be reflected onto the auxiliary camera and is used to determine the energy in a pulse. The remaining light will be focused onto the sample through the use of a microscope objective (100X Nikon CF160). The objective is mounted on a linear motorized stage (Zaber T-LSN025A) to allow focusing on the Z-axis. In order to mount and move the sample, a moveable stage is used (Physik Instrumente M686 PILine). A part of the light focussed on the sample will be reflected and detected by the objective. Thereafter, the reflected light will be focussed onto the main camera using a lens after being reflected by the second pellicle beam splitter. Thereby, the reflected ablation spot could be imaged [36].

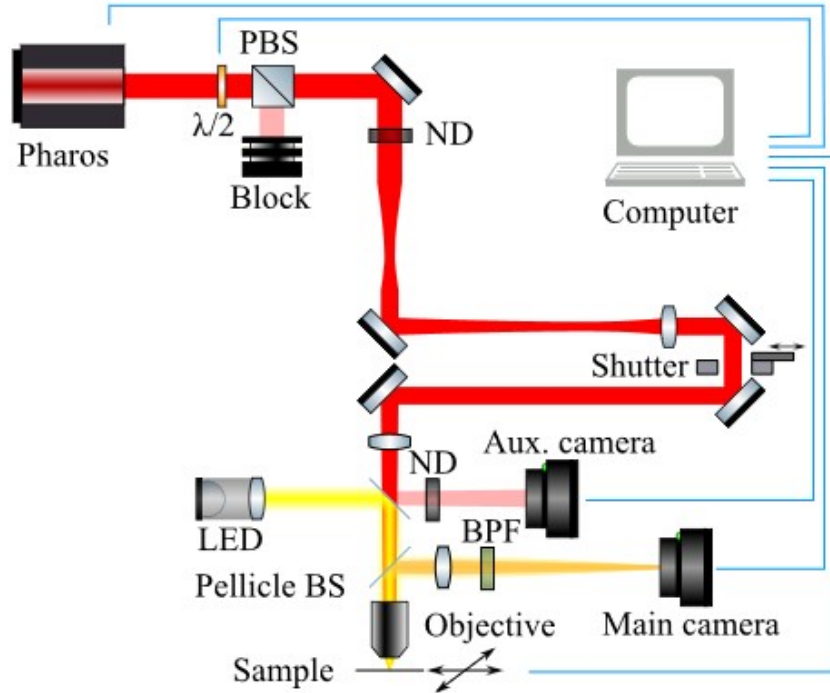


Figure 8: Reproduced with permission from [36]. A schematic of the experimental setup. An incident illumination of 1034 nm is used. $\lambda/2$: half-wave plate; PBS: polarizing beam splitter; ND: neutral density filters; Pellicle BS: Pellicle beam splitters; and BPF: bandpass filter.

When an experiment was performed with the setup (figure 8), the prepared BK-7 glass was placed in the sample holder. By utilizing the existing functions of the software for the setup, the surface of the sample could be detected. Then, the focus point could be moved in the x, y and z dimensions by moving the stage. This way, the focus point could be placed towards a chrome dot. This allows an easier retrieval of the ablation sites in different setups. The starting point of an experiment is based on an arbitrarily chosen position. Then, the coordinates for an experiment can be loaded in, these are relative to the starting point of an experiment.

Table 2: Settings used in the creation of an 8 by 8 laser engraved grid in the BK-7 glass.

<i>Parameters</i>	Exp1	Exp 2
Shape	Grid	Grid
Pulse strength (μJ)	0-1.1 (64 steps)	1.1
Total coordinates	64	64
Distance between sides (μm)	10	1.5
Pulses per coordinates	1	1-128 (64 steps)

Depending on the experiment, the method to create the list was different. The built-in software of the setup was able to create the coordinates and setting for an 8 by 8 grid. The settings of the experiments, in which a grid was used, can be seen in 2 as 'Exp 1' & 'Exp 2'.

In the case of 2D sub-surface laser engraving, the coordinates will be generated through the script as described in section 3.2.1. The settings of these experiments, where used in 2D sub-surface laser engraving can be seen in table 1, as 'Exp 1' and 'Exp 2', the coordinate lists should result in the letter 'R' at a depth of $100\mu\text{m}$.

In the case of 3D sub-surface laser engraving, the coordinates will be generated through the script as described in section 3.2.1. The setting of the experiments in which 3D sub-surface laser engraving was performed can be seen in table 1, as 'Exp 3' and 'Exp 4'. The coordinate lists should result in the letters 'H' at a depth of $250\mu\text{m}$ and a 'T' at a depth of $100\mu\text{m}$.

3.2.3 Bright-field transmission microscope

To visualise a sub-surface laser engraving described in the previous section, a bright field transmission microscope was used. The setup is schematically visible in 9. The setup consists of a Hamamatsu C11440 digital CMOS camera, with a field of view of 2048×2048 pixels and a pixel size of $0.065\mu\text{m}$. The used objective is 100x, therefore the full image seen through the Hokawo software is a square of 133.12 to $133.12\mu\text{m}$. To move the sample, a Thorlabs NanoMax TS MAX300 Series 3-axis flexure stage is used. For Illumination, a LED in the colour white was used. To inspect The BK-7 glass, it was placed inside a sample holder in the setup. Then, by adjusting the stage, and utilizing the chrome dots as a reference point, the focus could be set on the ablation sites. When the ablation site was in focus, an image could be captured using the built-in software. The images were then saved and processed using a tiff data type. Then, by using ImageJ [37], the data could be analysed.

3.3 Automatic differentiation ptychography

3.3.1 Ptychography setup

To capture diffraction patterns of the created 2 and 3D objects, a setup as seen in fig 10 was used. Here, the illumination source is a Cobalt Jive 100, which operates at a fixed wavelength of 561 nm . The source is a continuous-wave diode-pumped laser. Then, the laser is guided through a fibre onto a flippable diffuser. If the diffuser is flipped into position it will allow the usage of a speckle pattern for the probe, Otherwise, it will use a flat probe. Hereafter, the pinhole will, through the use of 2 lenses, be relayed onto the sample. The sample will be mounted on a moveable stage

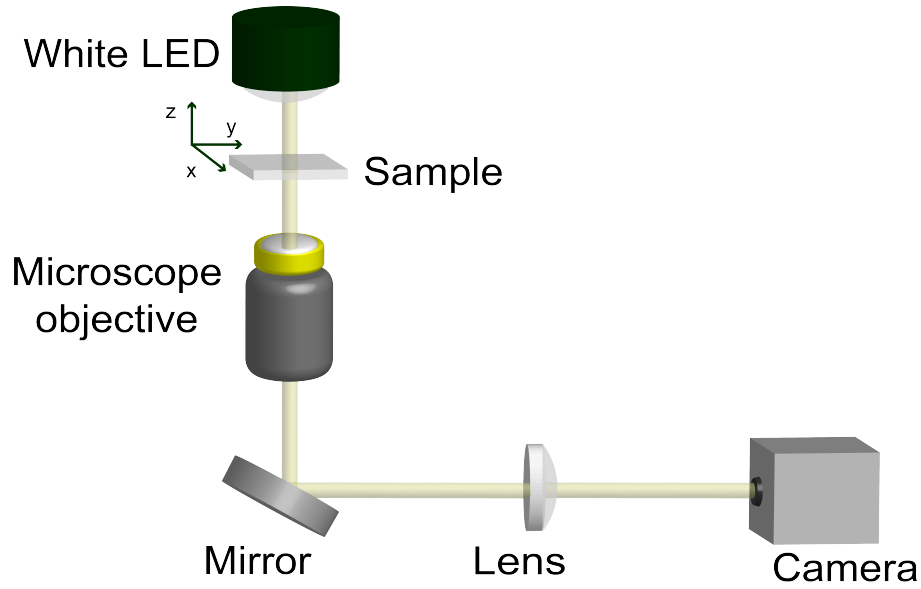


Figure 9: Schematic of the used bright-field transmission microscope using a 100X objective. The sample will be placed in a sample holder and by moving a stage the microscope objective can be focussed on the ablations.

(KST101), which allows the sample to be moved. Finally, the diffraction patterns will be collected by the detector (type Basler acA2440).

in total, 3 measurements were performed, for different engravings within the glass. The first measurement, further referred to as ptychography measurement one, was done by performing a calibration measurement and then scanning in a square grid of 2 mm around where the structure was supposed to be. The structure which was to be expected would be the letter 'R' (table 1 Exp 1), which was engraved at a depth of 100 μm . In the setup, a propagation distance of 6.2 cm was used with a pixel size of 3.45 μm . The diffuser was switched into place, thereby the probe used during the measurement was a speckle pattern. Then, the diffraction patterns were created by moving the stage and captured by the detector. the scanning patterns were saved along the mask, background, and scanning points in the form of a ptychogram file.

The second measurement, further referred to as ptychography measurement two, was done by performing a calibration measurement and then scanning in a square grid of 2 mm around where the structure was supposed to be. The structure which was to be expected would be the previously mentioned letter 'R' (table 1 Exp 2) and the letters 'T' & 'H'. The letter 'T' was engraved at a depth of 100 μm and the 'H' at 250 μm (table 1 Exp 4). The diffuser was switched into place and thereby using a speckle pattern. The used propagation distance between the glass and the camera was 6.2 cm and a speckle size of 3.45 nm. Then, the diffraction patterns were created by moving the stage and captured by the detector. These were then saved along the mask, background, and scanning points in the form of a ptychogram file (.HDF5) along the parameter file.

The third measurement, further referred to as ptychography measurement three, was done by performing a calibration measurement and then scanning in a square grid of 2 mm around where the structure was supposed to be. The structure which was to be expected would be the previously mentioned letter 'R' (table 1 Exp 2) and the letters 'T' & 'H' (table 1 Exp 4). The letter 'T' was engraved at a depth of 100 μm and the 'H' at 250 μm . For the creation of speckle patterns, the diffuser was switched into place and thereby using a speckle pattern. The used propagation

distance between the glass and the camera was 3.0 cm and a speckle size of 6.9 nm. These were then saved along the mask, background, and scanning points in the form of a ptychogram file (.HDF5) along the parameter file.

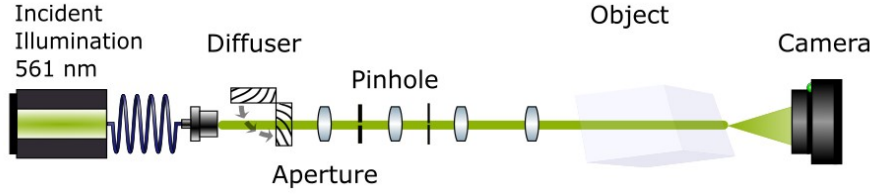


Figure 10: Schematic lensless imaging setup to create and collect diffraction patterns. Using the flippable diffuser, both structured and unstructured incident illumination (561 nm) can be used. The pinhole is relayed onto the object by the aperture and the 2 lenses, to illuminate the object. The diffraction patterns are then detected downstream through the camera.

3.3.2 Experimental reconstruction of experimental diffraction patterns using AD-based algorithm

To reconstruct the object and probe, an unpublished version of the AD-based framework, derived from Seifert et al [26], will be used. The reconstruction process has been described in section 3 utilizing the Adam optimizer [38] to reconstruct the probe and object. In total, there were 3 reconstructions run using the ptychogram and parameter files created as described in section 3.3.1. The corresponding files were loaded into the algorithm. The parameter file used can be seen in the appendix, and changes will be specified. If not mentioned in either case, then the default values were used.

The reconstruction of ptychography measurement 1 used a speckle probe and thus a weight mode probe of 2 was used, which was divided as 1/3 to 2/3. The sample type was 2D, with a background factor of 1.52. A learning rate for the sample and probe was for both 0.15. The sample-l1 regularizer was set to 0.02. The reconstruction of ptychography measurement 2 used a speckle probe and thus a weight mode probe of 2 was used, which was divided as 1/3 to 2/3. The sample type was 2D, with a background factor of 1.52. A learning rate for the sample and probe was for both 0.15. The sample-l1 regularizer was set to 0.02. The reconstruction of ptychography measurement 3 used a flat probe. The sample type was 2D, with a background factor of 1.52. A learning rate for the sample and probe was for both 0.15. The sample-l1 regularizer was set to 0.02.

The regularizer applies a parameter to the parameter being optimized, thus having an influence on the error function in the algorithm. By applying a regularizer, the potential reconstructions are limited. Applying a decay rate of 99%, allows the algorithm to function better. This, as the regularizes, will be varying during the optimization, ending at 37% of the start value. Doing so allow the algorithm to optimize for the error function more precisely. The learning rate for the probe and sample will let the algorithm update both during optimization. Then, for all reconstructions, the object, and probe were saved as NumPy. These could then be analysed through Fiji [39].

3.4 Simulating data and analysing

A simulation which mimics the ptychography setup as described in section 3.3.1 was made. The function of the simulation is to predict the influence of a change in parameters on the overall reconstruction quality. The scripts which are used in the simulation to create the diffraction patterns, reconstruct the object and analyse the reconstruction can be seen in the appendix. In this thesis, the main focus of the simulation will be to inspect the implementation of multiple layers and inspect the influence of the distance between layers. Therefore, for a range of 10 to 10 000 μm in 60 steps, the diffraction patterns will be simulated with only the distance between the layers changing. Then, by reconstruction of these simulated diffraction patterns, the layers should be retrieved. To determine the quality of the reconstruction, the reconstructed 2D layers can be compared to the known solution. The comparison can be done by the complex correlation function, which has been described in section 14. In this subsection, the required components to build a simulation will be provided. The components which are necessary to build and run the simulation are a sample, scanning points, a probe, a background, and a mask. Additionally, a list of parameters is required. By providing these, the model can be built, and diffraction patterns can be simulated.

3.4.1 3D object consisting of two 2D independent layers

The sample consists of two 2D layers independent of each other and thus forming a 3D sample. The layers will consist of commonly used images in ptychography. The first layer will be a cameraman and the second layer a mandrill. In order to prepare the original photo, the images have been grey-scaled, rescaled and padded to let the outside be 0. Then, the layer was transformed to be a phase object only by applying the sample as a phase. Therefore, the created 2D objects can be seen in fig 11, together creating a 3D object. This 3D object could then be initialized in the simulation. The layer closest to the illumination source was the cameraman and will be further referred to as layer 1. The layer closest to the detector was the mandrill and will be further referred to as layer 2.

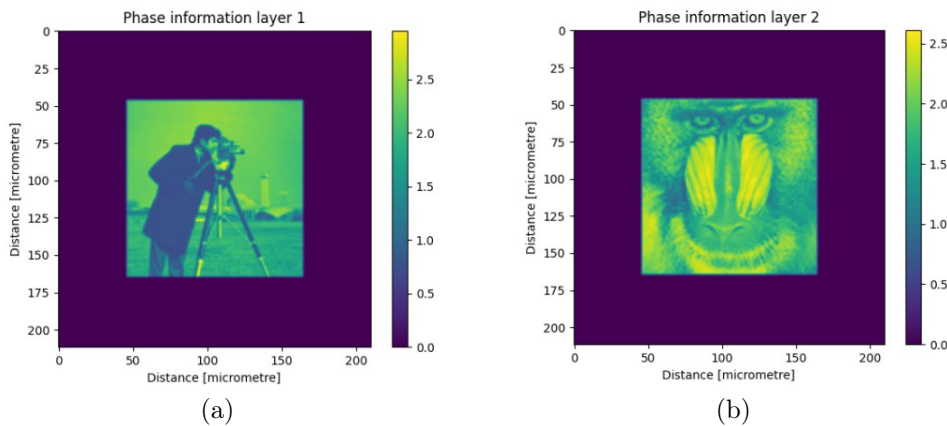


Figure 11: A simulated sample consisting of two layers. The first layer (a), closest to the illumination source, is a cameraman. The second layer (b), closest to the detector, is a mandrill. Both layers have an set amplitude component of 1's only

3.4.2 Fermat spiral to create scanning points

As stated, the simulation requires scanning points. The scanning points will serve as coordinates for the probe to illuminate the sample, creating diffraction patterns. As the amount of overlap correlates to the quality of the reconstruction, it is suspected that the 'optimal uniformness' could be reached using a Fermat spiral to minimize scanning time while maintaining an ideal overlap [40]. The scanning points required to create diffraction patterns were created by employing the formula for the Fermat spiral (equation 15) with $\theta = n\theta_0$. In the function, c is the radius divided by the square root of the total points. Furthermore, n is the index number of the spiral and $\theta_0 = 137.508$. θ_0 is considered the golden angle, as it divides a circle in the golden ratio of $\theta = (1 + \sqrt{5})/2$ [41]. This formula will give the coordinates in polar coordinates.

$$r = c\sqrt{n} \quad (15)$$

$$x = \cos(\theta) * r \quad (16)$$

$$y = \sin(\theta) * r \quad (17)$$

These polar coordinates can then be transformed into Cartesian coordinates by employing the equations seen in 1617. In order to create the scanning positions, the implementation requires the total amount of points, the offset for the spiral centre and the max radius in millimetres. By using a total of 150 scanning points and a radius of 3.51 with the centre of the coordinates at 0.0, the following scanning grid was created 12. These settings allow an overlap of 79% in the diffraction patterns.

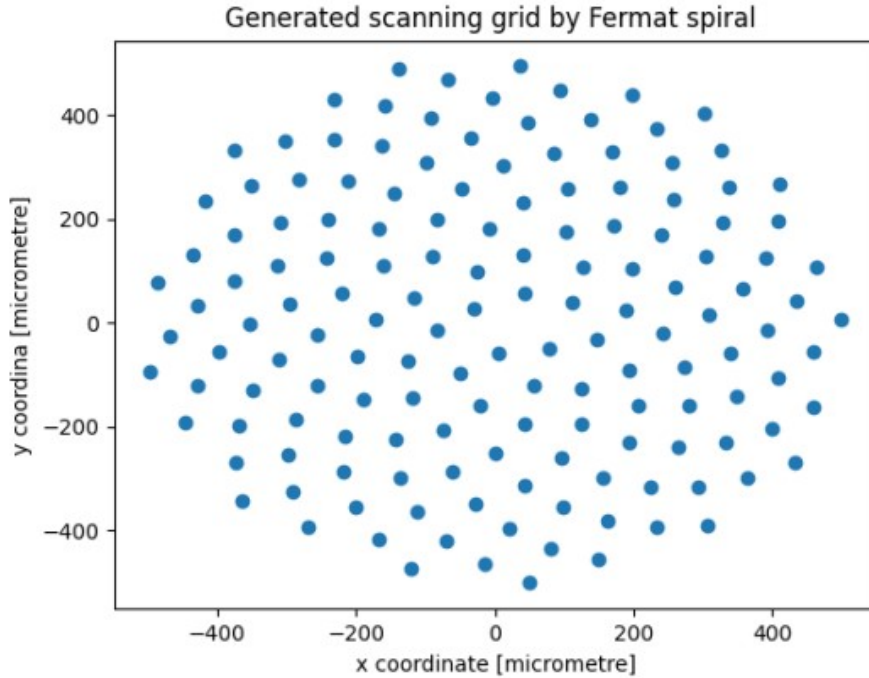


Figure 12: The 150 simulated Scanning positions based on the Fermat spiral [40]. At each coordinate, a probe will be placed in the simulation to mimic the illumination source and generate diffraction patterns.

3.4.3 Flat probe as illumination source

The function of the probe is to mimic an illumination source. By placing a probe at each scanning point, the sample will be illuminated, and a diffraction pattern will be created. In these simulation experiments, a probe will be used. The creation of the probe consists of multiple steps. The first step is probe sampling based on the number of pixels and pixel size. In the simulations performed, a pixel size of $6.9\text{ }\mu\text{m}$ was used with a pixel number of 1024.

By using these coordinates and the given size of the probe, a flat probe can be generated. This general probe is then reshaped to the correct shape. Then, the absolute of the probe is taken to create the amplitude aspect of the probe. Then, by applying a Gaussian filter [42], the edge is made smooth to avoid a sharp cut-off. Furthermore, a quadratic phase is assigned to the probe, to allow a phase-only object to contribute to the diffraction pattern. By creating a grid of 1024 steps linearly divided between $-\pi$ & π a phase was added to the probe.

This way, the probe as seen in figure 13 was created. As seen, the probe has both amplitude and phase information. The phase will range from zero to π .

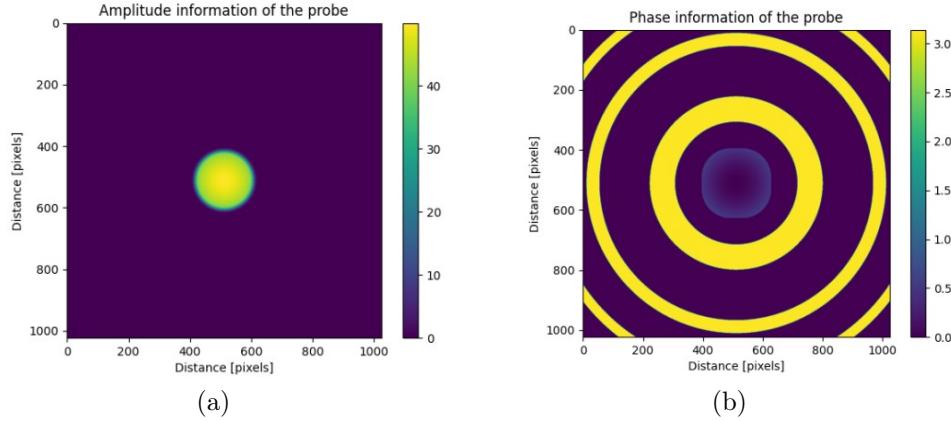


Figure 13: The flat probe, consisting of both amplitude (a) and phase (b) components. A pixel in here is $6.9\text{ }\mu\text{m}$.

The mask in the ptychogram is used to remove certain pixels in the diffraction pattern from optimization and will be set to 1's everywhere. The background can be used to remove the background of the diffraction patterns. However, in the simulation, there should be no background in the simulation and therefore the values are set to 0's.

3.4.4 Simulating diffraction patterns and reconstructing the 3D object

The simulation created diffraction patterns and reconstruct the objects in the following way. First, the scanning points, sample, probe, mask, and background were initialized. Then, the parameter list, as seen in the appendix, was initialized. If Thereafter, the simulation was started, starting with a distance between layers of 10 mm. The created diffraction patterns were temporarily saved and used directly used to reconstruct the object and thus each layer. The reconstruction was run with the parameter file for the numerical data can be seen in the appendix. Additionally, a regularizer for the sample of 0.01 was used. If not mentioned, then the default values were used. For the reconstruction, the probe was loaded in to increase the chance of convergence and prevent phase drift. The reconstructed layers were then

saved as a NumPy file (.npz). Then, the distance between layers was updated, and the process was repeated, resulting in 60 hdf5 files containing the reconstructed layers for each distance between the layers. In total, the distances between the layers were ranging from 10.0 to 100 000 μm , being gradually increased in 60 steps.

4 Results and discussion

4.1 Determining the laser parameters

In this section, the ablation for the BK-7 glass sample will be inspected. The results were used to determine the parameters for a sub-surface ablation experiment. The parameters are required to create a multidimensional object to allow ptychography. First, the required pulse energy will be inspected to notice any damage inside the BK-7 glass, by varying the pulse energy. This can be seen in section 4.1.1. Then, the experiment will be repeated by using the chosen pulse energy, varying the number of pulses per ablation site, seen in section 4.1.2. The coordinates of these experiments will be provided by the built-in software of the setup (section 3.2.2).

4.1.1 Determining damage threshold and visualizing damage in BK-7 glass in X,Y dimensions using a single pulse

To determine the energy per pulse required, an 8 by 8 2D grid was created through laser engraving at a depth of 100 μm . In the experiment, the pulse energy gradually increased from, 0 to 1.1 mJ in 64 steps for a single pulse. The grid was made by moving the sample vertically after each ablation and then turning horizontally and moving back vertically until the 8 by 8 grid was made. By using the bright-field transmission microscope as described in section 3.2.3, the damage could be inspected. To analyse the data, 4 data points were taken in the grid at various points in the graph to determine the influence of increasing energy. These 4 points and the 8 by 8 grid can be seen in figure 14. Through analysing the 4 points for their respective size, the influence of the increase in energy can be determined. As seen in fig 15 using a higher energy single pulse will result in an increase with respect to the X & Y dimensions. It can be seen that ablation starts to occur while using a pulse strength of at least 0.3 μJ /pulse. This would correlate to an ablation size of 0.7 μm . For the maximum pulse energy used (1.1 μJ), an ablation size of 1.7 μm can be seen. However, to allow the biggest refractive index change, for all further laser engraving a pulse energy of 1.1 μJ was used. In theory, determining the influence of a single pulse containing higher energy in the Z-dimension is possible, if all sides of the glass would be transparent. Then one could analyse the influence of increasing energy with a single pulse by turning the glass sideways and visualizing through the side, rather than the top. In practice, however, the BK-7 glass is opaque on the side and therefore there can be no conclusion drawn regarding the Z dimension. Based on the finding by Petrovic et al, there should be filamentation occurring resulting in a However, the expectation is that with increasing energy, the size will also increase for the Z dimension. The finding of the increase of the size in the X&Y is in accordance with the finding by Petrovic [18].

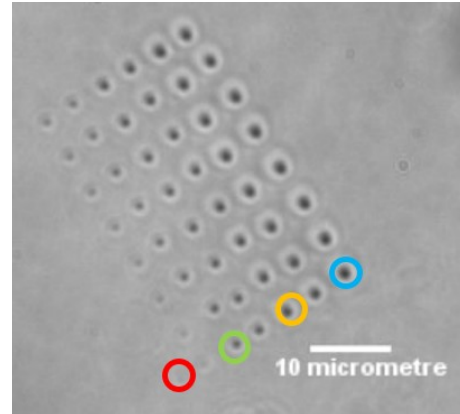


Figure 14: Bright-field microscope image of the 8 by 8 sub-surface laser engraved grid of ablation sites at 100 μm . The energy per ablation site was increased from 0 to 1.1 μJ in 64 steps.

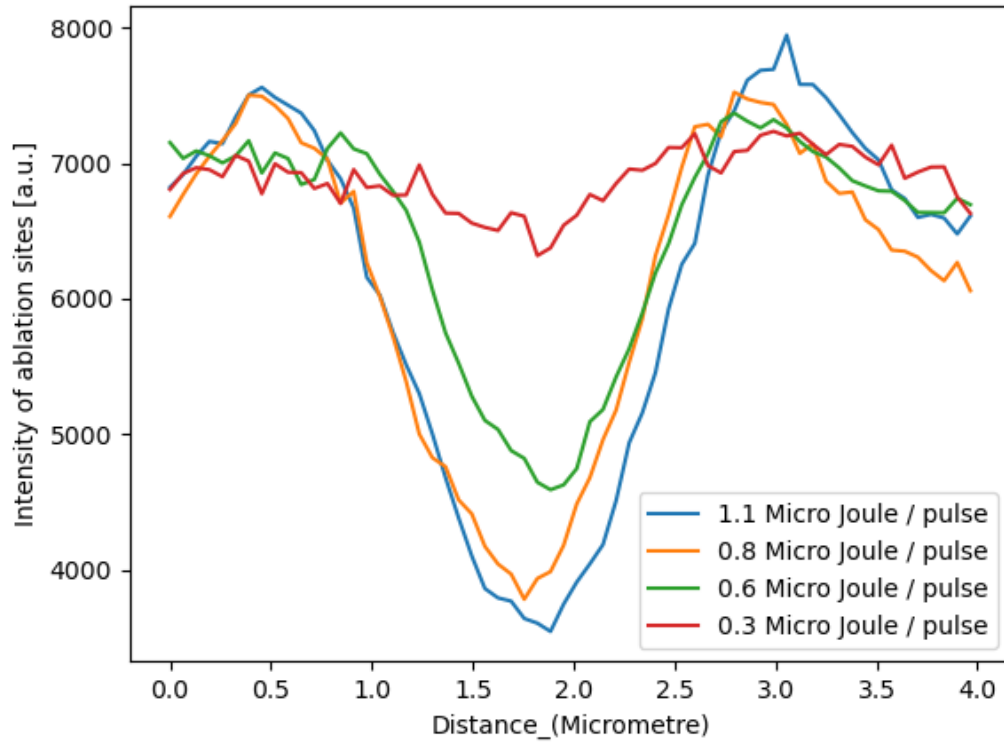


Figure 15: Size of an ablation site in μm for varying pulse energies versus the intensity based on figure 14.

4.1.2 Influence of multiple pulses for the size in XY dimension of BK-7 glass

To determine the influence of multiple pulses rather than a single pulse, a second 8 by 8 grid was created through laser engraving at a depth of $100\mu\text{m}$. The number of pulses was increased while keeping the pulse energy constant ($1.1\mu\text{J}$). The grid was made by moving the sample vertically after each ablation and then turning horizontally and moving back vertically till the 8 by 8 grid was made. The number of pulses per ablation site increased gradually from 1 to 128 in 64 steps. By using the bright-field transmission microscope as described in section 3.2.3, the damage could be inspected. To analyse the data, 5 data points were taken in the grid at various points to determine the influence of multiple pulses. These 5 points, along the 8 by 8 grid, can be seen in 16.

Through analysing the 5 points for their respective size, the influence of multiple pulses per ablation site can be determined. As seen in fig 17, using more pulses per ablation site results in a bigger size in the X&Y dimension. Additionally, the $1.1\mu\text{J}$ pulse gives the same ablation size as in the previous section, indicating the number of pulses indeed increased. Furthermore, for the highest number of pulses per ablation site (128), the size of the ablation is $6\mu\text{m}$. The BK-7 is able to withstand multiple pulses and therefore can be used to create more damage inside the glass. Therefore, the sub-surface limitations will lie in the stability of the sample, rather than the available power of the used setup. In theory, determining the influence of multiple pulses is possible for the Z-dimension, if all sides of the sample would be transparent. Then one could analyse the influence of increasing energy with a single

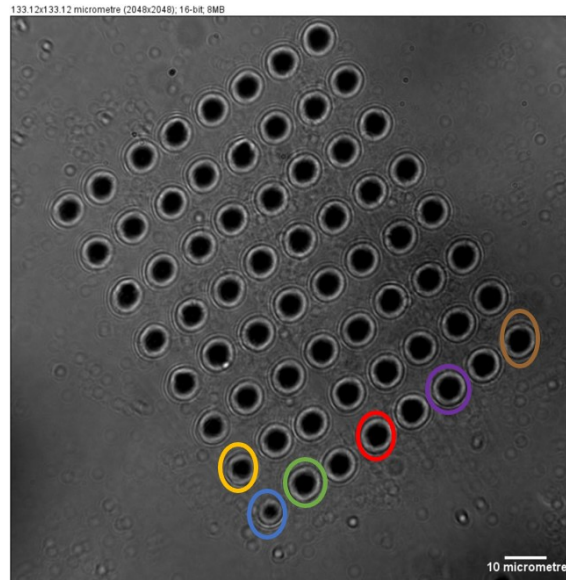


Figure 16: Bright-field microscope image of the 8 by 8 sub-surface laser engraved grid at a depth of $100\text{ }\mu\text{m}$ using a pulse energy of $1.1\text{ }\mu\text{J}$. The number of pulses per ablation site was increased from 1 to 128 in 64 steps.

pulse by turning the sample sideways and analysing through the side, rather than the top. In practice, the BK-7 glass is opaque on the side and therefore there can be no conclusion drawn regarding the Z dimension. Nevertheless, one would expect filamenting to start occurring for multiple pulses, but no statement regarding this effect can be made with the available data. However, the expectation is that with increasing energy, the size would also increase for the Z dimension.

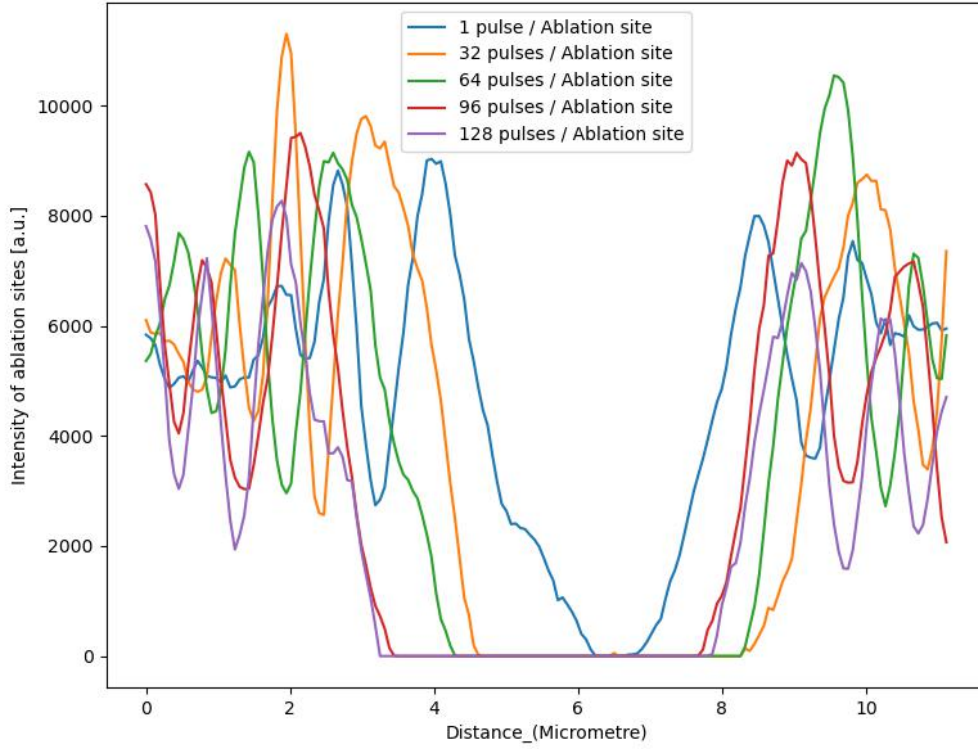


Figure 17: Size of an ablation site in μm for a varying number of pulses versus the intensity.

4.2 Sub-surface laser engraving for 2D ptychography

In this section, it will be inspected if sub-surface laser engraving can be used for creating samples reconstructable by ADP. First, the script to transform a 2 or 3D model into a list of coordinates will be validated in combination with the setup described in 3.2.2 by performing an ablation experiment using the coordinates gained from a 2D model. Finally, the sub-surface engraving will be placed in the ptychography setup (section 3.3.1) to capture diffraction patterns of the 2D object and be reconstructed using ADP.

4.2.1 Validating software to perform sub-surface laser engraving

The creation of the grid was done with the already present software for the laser setup. However, the capability to convert a two- or three-dimensional model to a list of coordinates of the created script has not been tested. Therefore, the coordinate lists of the letter 'R' (table 1 Exp 1 and 2) were used to laser engrave at a depth of $100\mu\text{m}$ in the BK-7 glass sample.

As seen in figure 18, the laser engraving was successful, as in both figures the letter 'R' can be seen. Therefore, the created script to transform a two- or three-dimensional model into a list of coordinates while specifying the pulse strength, distance between coordinates and indirectly the total coordinates is functioning as intended.

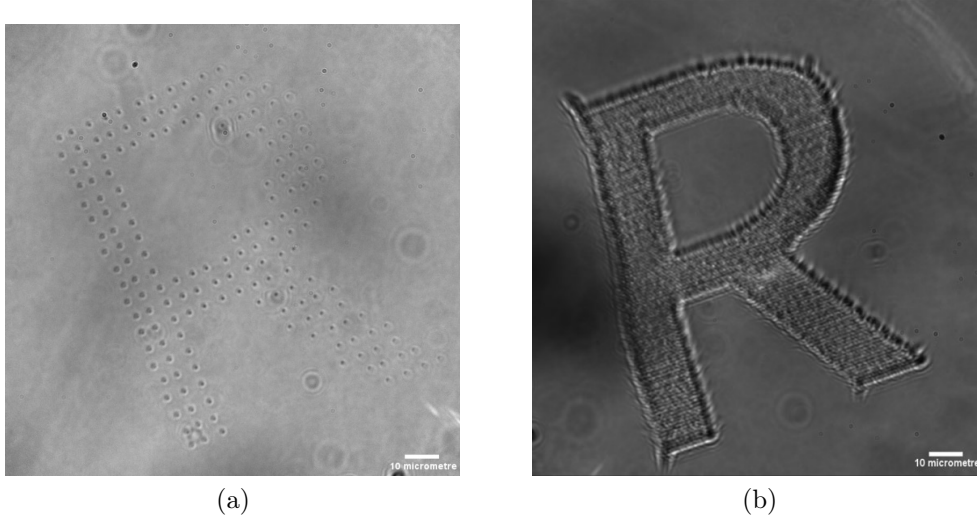


Figure 18: Bright-field microscope images of the laser engraving of the letter 'R' inside the BK-7 glass. In (a), the engraving is based on the coordinate list from table 1 Exp 1. In (b), the engraving is based on the coordinate list from table 1 Exp 2.

4.2.2 2D Ptychography measurement and reconstruction

Using the sub-surface laser engraved letters 'R', a ptychography measurement was performed and attempted to reconstruct the 2D objects through ADP. The reconstruction of the probe can be seen in figure 19.

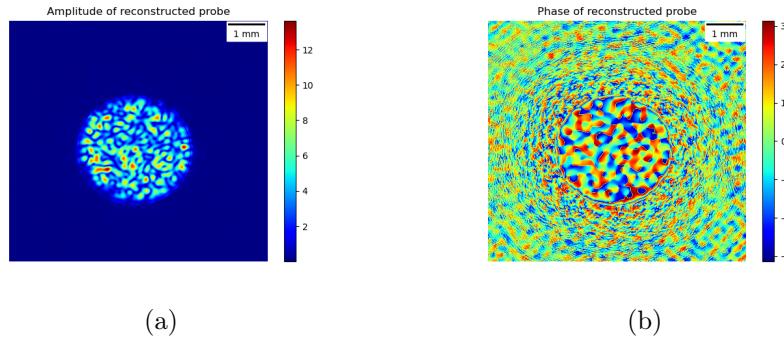


Figure 19: The amplitude (a) and phase (b) of the reconstructed probe in the reconstruction described in section 3.3.1 for the 2D engraved letter 'R'.

The patterns of both amplitude and phase are due to the speckle pattern used, and the probe is reconstructed well, thus the reconstruction converged for the probe.

Then, the reconstructed object can be inspected, the reconstructed data was saved and exported to Fiji. this leads to figure 20. Here, only one letter 'R' is can be seen, mainly due to the amplitude reconstruction. This is due to the phase reconstruction showing a structure but without prior knowledge, it cannot be claimed to be an 'R'. However, it shows a structure created through sub-surface laser engraving. Nevertheless, the engraving based on the parameters of table 1 Exp 1 did not result in a visible structure and is thus not suited for creating a reconstructable 2D object, whereas the parameters of Exp 2 are.

However, the 2D engraving based on the parameters of table 1 Exp 2 is for both

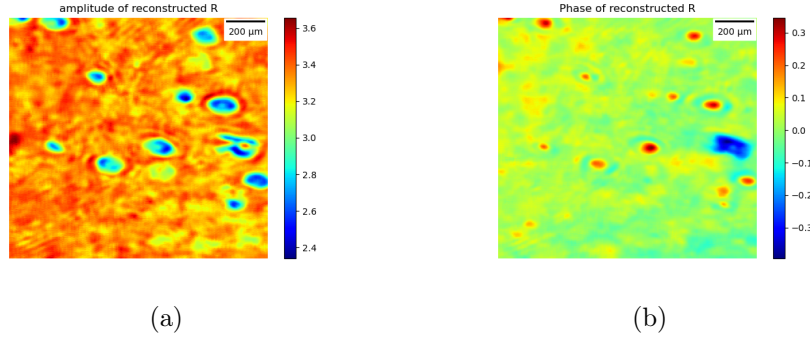


Figure 20: The amplitude (a) and phase (b) of the reconstructed object in the reconstruction described in section 3.3.1 for the 2D engraved letter 'R'.

the probe and object well enough to reconstruct them.

The difference between the parameters for the engravings of the letter 'R' could explain the failed versus successful reconstruction of the object. As seen in (a), the structure does not seem to be continuous, thus the distance between ablation sites should have to be increased to solve this. Additionally, the contrast to (b) could be improved by increasing the number of pulses per coordinate. However, based on these 2 engravings it is impossible to say what the minimal distance between coordinates, the number of pulses per coordinate and the number of ablation sites have to be, to get a successful reconstruction of the 2D object.

Nevertheless, sub-surface laser engraving has been shown to be able to successfully create 2D objects to be used as test samples for ptychography measurements. Even if the phase of the letter 'R' could not fully be reconstructed, sub-surface laser engraving shows great promise to be able to do so.

4.2.3 3D ptychography measurement and reconstruction

Section 4.2.2 described the successful reconstruction of the letter 'R' as a 2D object. However, after the implementation of the expanded angular spectrum method, the reconstruction of 3D objects should be possible. The expectation is that by using the same settings for the successful 2D reconstructed letter 'R', a third dimension could be added. By adding a third dimension to the sample, the to-be-reconstructed object would increase from 2D to 3D. Therefore, by choosing 2 two-dimensional structures on top of each other independent of each other, a three-dimensional structure can be created through sub-surface laser engraving. To get a good grasp on the capability of the reconstruction, the letters 'T' & 'H' were decided. The use of these letters will allow a part of the bottom 'H' to be hidden behind the 'T'. These regions are expected to show signs of crosstalk in the reconstruction.

Then, through sub-surface laser engraving, the 'T' & 'H' based on the parameters in table 1 Exp 3 were engraved in the BK-7 glass. During the experiment, it became apparent the used parameters would be too destructive to engrave the 'T' on top of the 'H'. After finalizing the 'H', the engraving setup could not focus on the sample, thus it was not possible to use these settings to create a 3D object. Therefore, a new experiment was performed based on the parameters in table 1 Exp 4, in which the distance between dots was increased and the number of points reduced. The total size however was kept the same, therefore the changes will result in a less dense structure. The engraving of the letters 'T' & 'H' is successful, as seen in figure 21. Due to the limited DOF of the bright-field microscope, the 'H' could not be focussed upon, however, the letter can still be seen and thus is inside the BK-7 glass.

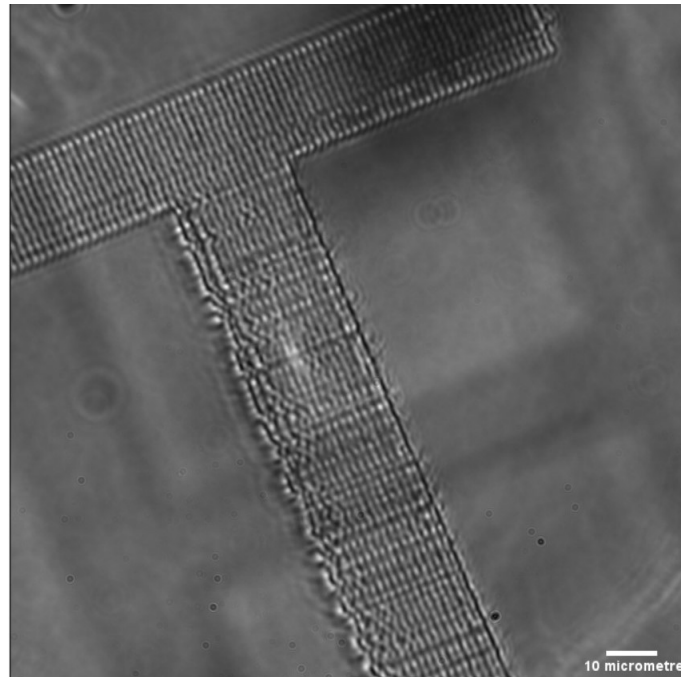


Figure 21: Bright-field microscope images of the laser engraving of the letters 'T' & 'H' inside BK-7 glass. The engraving is based on the coordinate list from table 1 Exp 4.

Using the sub-surface laser engraved letters 'T' & 'H', a ptychography measurement was performed and attempted to reconstruct the 3D objects through ADP for a propagation distance of 6.2 cm and a pixel size of 3.45 μm . The reconstruction of the probe can be seen in figure 22.

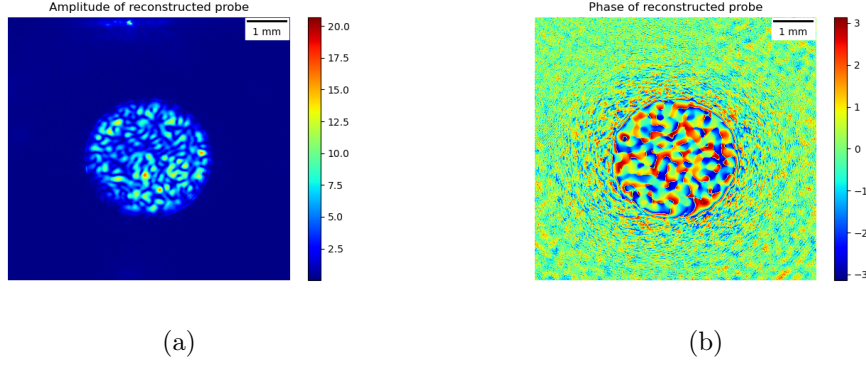


Figure 22: The amplitude (a) and phase (b) of the reconstructed probe in the reconstruction described in section 3.3.1, measurement 2, for the 3D engraved letters 'T' & 'H'.

The patterns of both amplitude and phase are due to the speckle pattern used, and the probe is reconstructed well, thus the reconstruction converged for the probe.

Then, the reconstructed object can be inspected, the reconstructed data was adjusted to focus on where the object should be and saved, to be exported to Fiji leading to figure 23. Both the letters 'T' & 'H' can be clearly seen on top of each other in both figures, although more noticeable for the amplitude reconstruction. For both the amplitude and phase of the 3D object, one could see that they are in different layers by the lower intensity of the lower layer ('H'). Nevertheless, As the reconstruction attempting to create multiple layers did not work out, even though the objects are 3D, the reconstructed structures are shown in 2D. Interestingly, the letter 'R' as seen previously can again be seen in both the amplitude and the phase. However, in the phase reconstruction, more distinguishably an 'R' can be spotted. The most likely reason could be the difference in parameters used, as the optimal parameters are difficult to determine to the number of variables possible to be twisted.

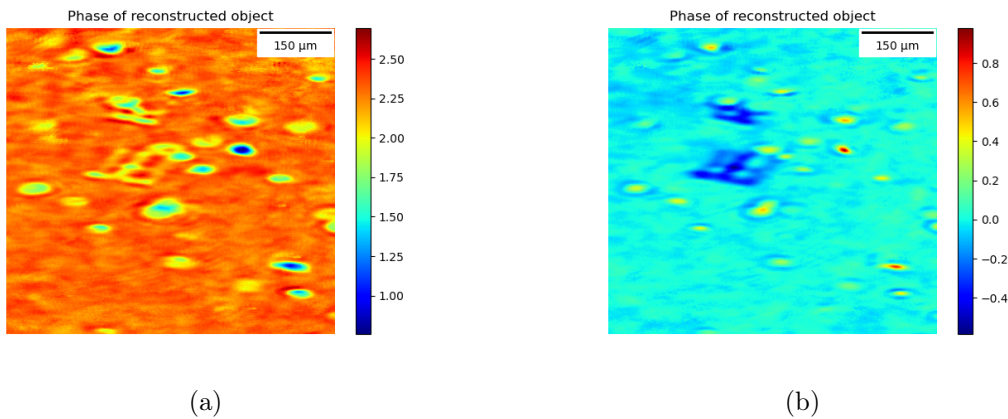


Figure 23: The amplitude (a) and phase (b) of the reconstructed object in the reconstruction described in section 3.3.1, measurement 2, for the 3D engraved letter 'T' & 'H'.

By using the phase image of the reconstructed 'T' & 'H' in combination with Fiji and the known pixel size ($3.45\ \mu\text{m}$), a graph of the phase shift versus the distance

in micrometre can be made, as seen in figure 24. An average of 5 pixels was used to create the graph. Here, the line was selected to make sure there were no overlapping regions included. By applying the 10-90% resolution [43], the resolution of the reconstruction for the laser-engraved object is $23\text{ }\mu\text{m}$.

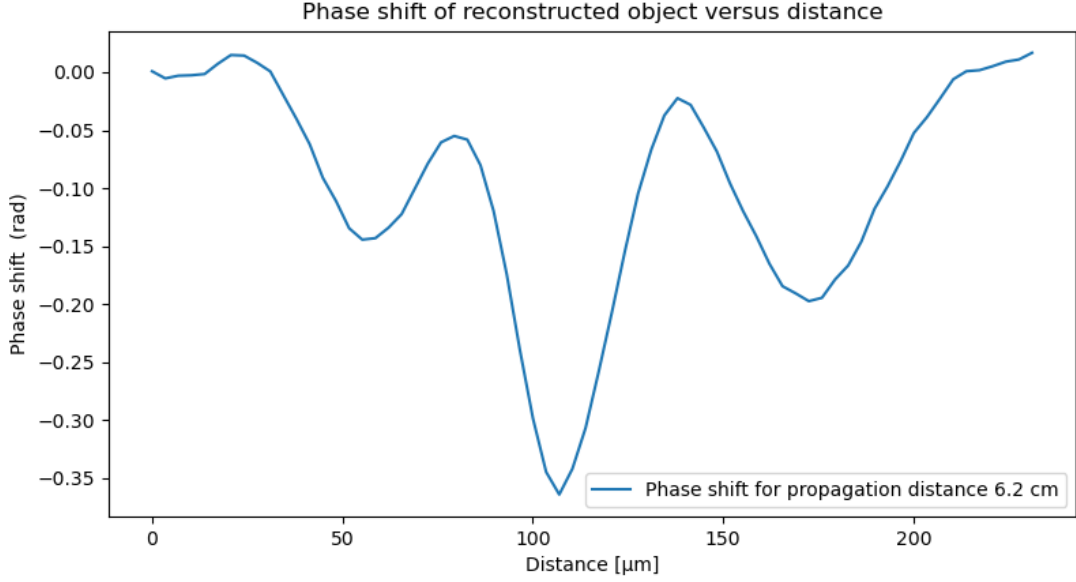


Figure 24: Phase shift of the reconstructed object of the laser engraved 'T' & 'H' for a propagation distance of 6.2 cm. The corresponding NA is 0.09

This indicates that the sub-surface laser engraving indeed can be used to create phase objects in 3D. To further improve the resolution, the same experiment can be done, but with a lower propagation distance and bigger pixel size. This will result in an increased NA, potentially allowing a better resolution.

Thus, based on ptychography measurement 3, as described in section 3.3.1, the same process has been performed. The probe in this case is a flat probe, due to the speckle probe exceeding the computational available memory. Reconstructing resulted in the probe look as seen in figure 25. Both seem to be converged, so the reconstructed objects can be visualized.

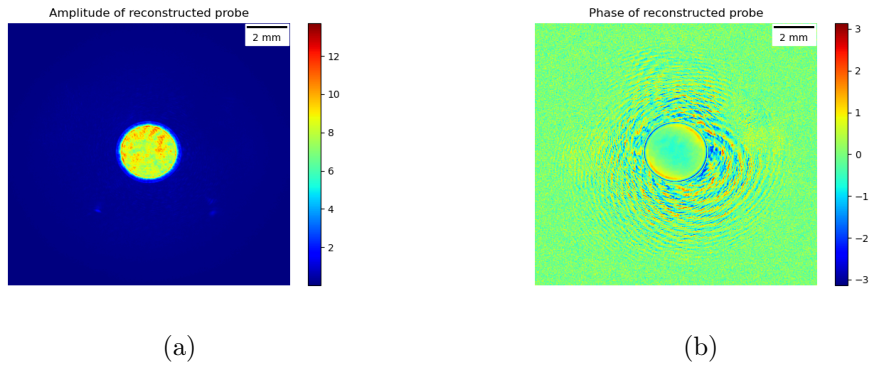


Figure 25: The amplitude (a) and phase (b) of the reconstructed probe in the reconstruction described in section 3.3.1, measurement 3, for the 3D engraved letters 'T' & 'H'.

The reconstructed data was adjusted to focus on where the object should be and

saved, to be exported to Fiji. this leads to figure 26. Both the letters 'T' & 'H' can be clearly seen on top of each other in both figures, with a seemingly higher resolution, as expected.

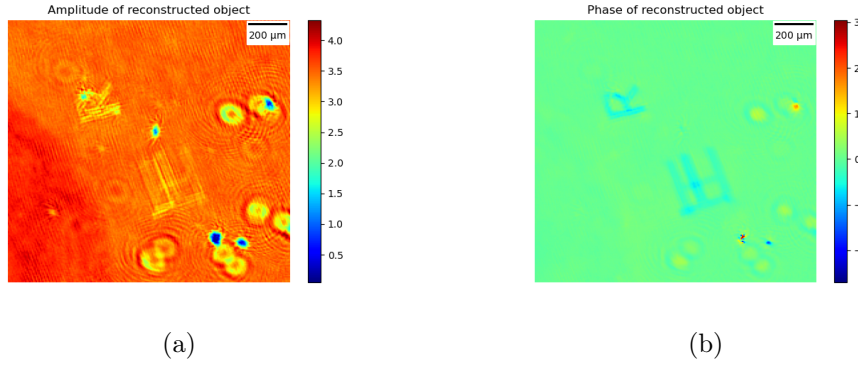


Figure 26: The amplitude (a) and phase (b) of the reconstructed object in the reconstruction described in section 3.3.1, measurement 3, for the 3D engraved letters 'T' & 'H'.

To validate this, the phase shift can be inspected by using the phase image of the reconstructed 'T' & 'H' in combination with Fiji, the graph as seen in figure 27 can be made. An average of 5 pixels was used to create the graph. Here, the line was selected to make sure there were no overlapping regions included. By including the phase shifts of the reconstruction for the propagation distance of 6.2 cm, a comparison can be made. By applying the 10-90% rule [43], a resolution of 10 μm.

In the end, the reconstruction of the experimental data did not work to recreate the engraved 'T' & 'H' in 3D. However, the 3D structure could well be reconstructed in both phase and amplitude for different propagation distances. A reason the reconstruction in 3D did not work is due to the chrome layers on the BK-7 glass. They served their purpose to find the ablation sites, but it could be causing the algorithm to lock onto them due to them being strong amplitude objects. Hence, it would be interesting to either remove them altogether or use them to test the framework. In order to use them, 2 chrome dots could be placed on both sides of the BK-7 glass, where they are slightly overlapping. Then, by performing a reconstruction, the dots could potentially be found in different planes. A different approach to testing the framework would be by increasing the size of the laser-engraved structures and removing the chrome dots. This should ensure the framework lock-on to the engravings rather than the chrome dots. However, the engraving would then be time-consuming and could potentially destroy the glass.

A definite solution would be to create a simulation which is able to reconstruct artificial samples. These could then easily be optimized and made as big as required.

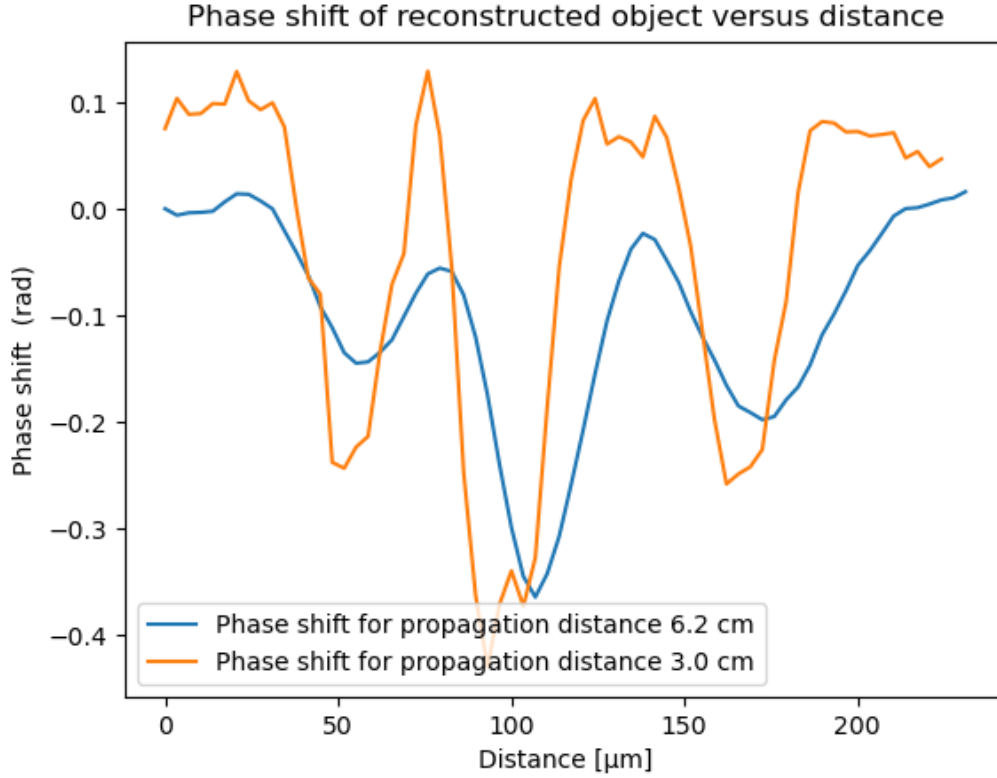


Figure 27: Phase shift of the reconstructed object of the laser engraved 'T' & 'H' for a propagation distance of 3.0 cm and 6.2 cm. For a propagation distance of 6.2 cm, The NA is 0.12. For a propagation distance of 3 cm, The NA is 0.03.

4.3 3D object reconstructed based on numerical data

As the experimental reconstruction did not converge for the 3D objects, a simulation is built to evaluate the reconstruction of two layers. Using the reconstructed objects as described in section 3.4, the correlation to the ground truth can be calculated using the complex correlation function (section 14). The reconstructed objects were corrected for drift, even though a fixed probe was used for the reconstructions. For all distances, the correlation between the respective layer and the real solution was determined and plotted in the top of figure 28. Furthermore, the correlation between both ground truths is included to function as a baseline.

As seen, the quality of the second layer (red line) seems to remain nearly the same in quality for the variation in distance between layers. However, the first layer (blue line) tends to increase for a larger distance between layers. Interestingly, the correlation does not smoothly increase as there are steps in which the correlation decreases. A reason could be the Adam optimizer not finding the global minimum but being stuck at a local minimum, preventing the best possible reconstruction to be reached. However, a correlation coefficient of greater than 0.94 for a very wide range of distances is amazing, even if the correlation of the known solution is already 0.72. Hence, it would be interesting for the smallest and biggest distance between layers, to visualize the corresponding layers. As the layers were initially only phase objects, only the phase components are shown in figure 29 compared to the known solution.

Upon visually inspecting the figure, a few things can be noticed for both dis-

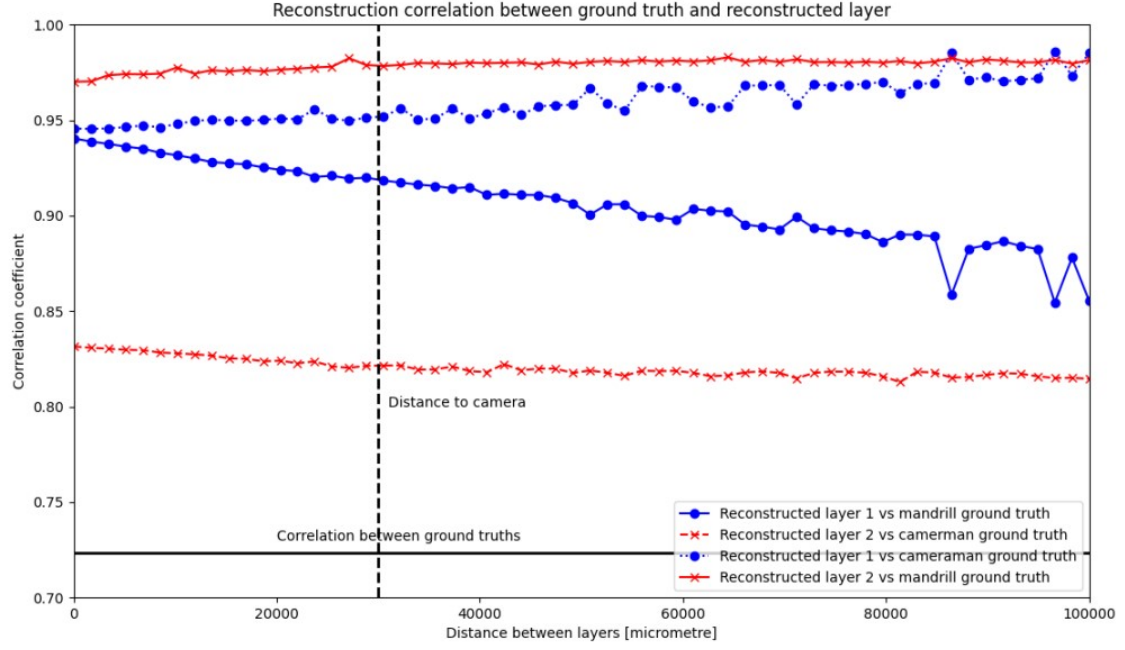


Figure 28: Correlation coefficients for the respective reconstructed layer and for both the known solution of this layer and the opposite layer based on the complex correlation function (section 14 versus the distance between layers. The dotted vertical line is the distance between the second layer and the camera (3 cm. The straight black line is the correlation between the known solution for both layers, serving as a baseline.

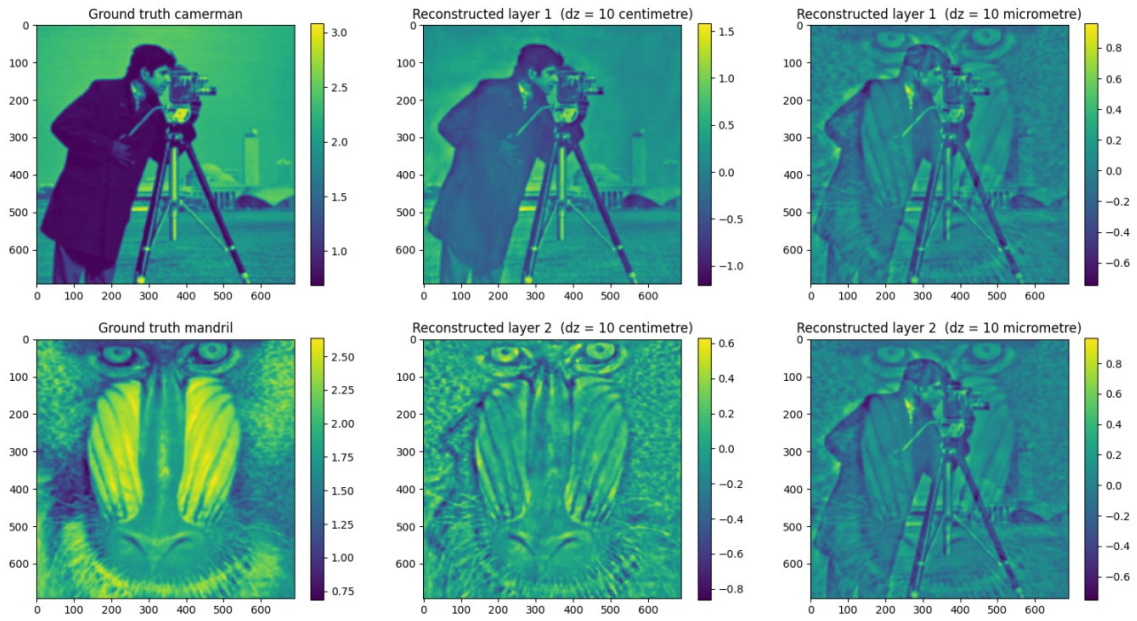


Figure 29: For only the phase components, a comparison of the ground truth of layers 1 & 2 versus the corresponding reconstructed layer for the smallest and longest distance between layers.

tances. When looking at the closest distance between layers $10\mu\text{m}$, barely any difference between the two reconstructed layers can be detected. as both show a lot of resemblance to both ground truths. For a distance of 10cm between layers, the reconstructed layers resemble the ground truth nearly perfectly. Especially the first layer, which only seems to have a certain glow to the cameraman, but no features of the mandrill. For the second layer, however, a part of the jacket from the cameraman seems to be in the reconstructed layer. These features should not be there and thus will contribute to a decrease in correlation. Furthermore, the improvement is quite noticeable when visually inspecting the layers for both distances. Therefore, the difference between the layers does not suggest a very small improvement of 0.04 in correlation.

As it can be seen that for a $10\mu\text{m}$ distance between layers, both the cameraman and mandrill end up in both reconstructed layers, it would be interesting to see how well the reconstructed layers correlate to the opposite ground truth. Therefore, these complex correlation coefficients were calculated. By using these correlations and the correlation coefficient for the correct combination of reconstructed layer and ground truth, the bottom part of figure 28 can be made.

Here, the straight blue line is the correlation coefficient between the reconstructed first layer and the ground truth of the second layer. The dotted blue line is the correlation between the reconstructed first layer and the ground truth of the first layer. The dotted red line is the correlation coefficient between the reconstructed second layer and the ground truth of the first layer, whereas the straight red line is the correlation coefficient between the reconstructed second layer and the ground truth of the second layer. It can be seen that the correlation to both layers is connected. When the second layer increases in correlation with the known solution, the correlation to the false ground truth decreases and vice versa. The difference for the layers however remains stable, as the second layer seems less dependent on the distance between layers for the correlation, and thus not much of the cameraman ends up in the second layer. The most interesting finding in this graph, however, is the first layer correlations. The correlation at the $10\mu\text{m}$ distance between layers is barely different between the correct layer and the wrong layer. This indicates there is indeed a significant amount of mandrill in the first layer, which could indeed be seen in the visualization of the layers (figure 29). Again, the correlation for the layer seems to be connected due to the correlation coefficient shifting equally on opposite sides. Eventually, the layer will reach the same correlation to the known solution as the second layer, but the correlation to the wrong ground truth will not match the second layer correlations. Therefore, for the entire range of distances between the layers, the first layer will contain more mandrill than the second layer will contain the cameraman.

So far, only the phase components have been considered for the reconstructed objects. However, even if the ground truth did not have an amplitude, the reconstruction still tried to retrieve the amplitude component. Therefore, the ground truth of the amplitude component can be visualized next to the smallest and longest distance between layers, as seen in fig 30. It can be seen that even though the ground truth of both layers is the same. the reconstructed layers still show some resemblance to the cameraman and mandrill. Again, the longest distance seems to show a significantly better reconstruction than the smallest distance, but both are nowhere near the ground truth. Therefore, it is uncertain why the correlation coefficient is nearly 1, as that would mean the reconstructed layers would be identical to the ground truth.

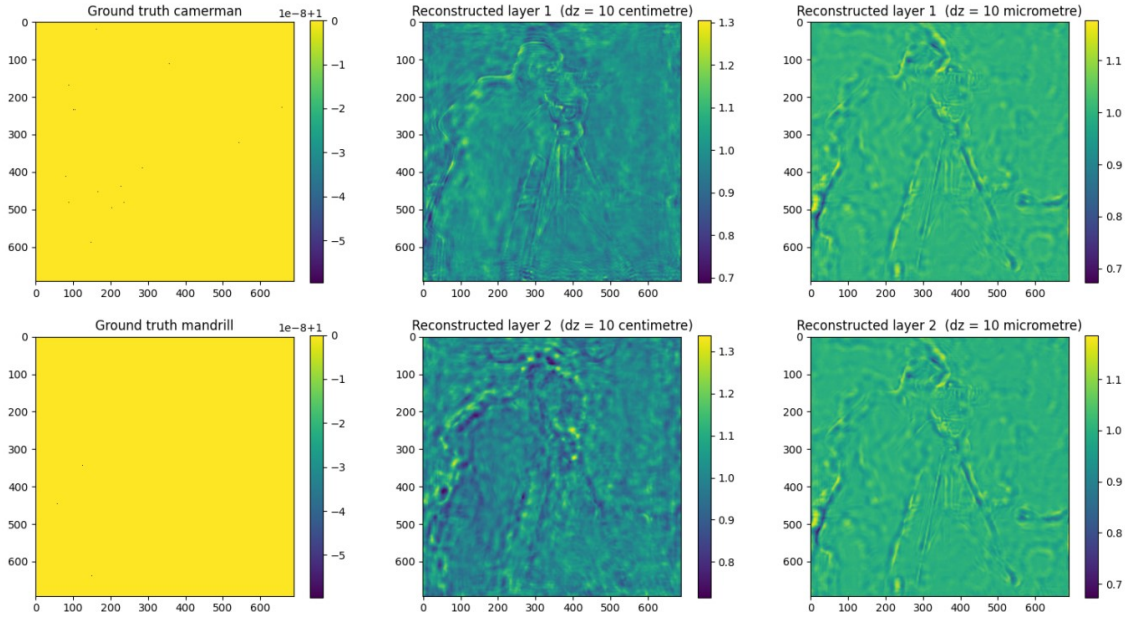


Figure 30: For only the amplitude components, a comparison of the ground truth of layers 1 & 2 versus the corresponding reconstructed layer for the smallest and longest distance between the layers.

Nevertheless, as the correlation between the ground truths already being 0.72, the coefficient approaching 1 could be explained. Although, visually inspecting the phase of the reconstructed layers showed indeed a great similarity to the ground truth, but also signs of the wrong sample ending up in the layer. The reason for the wrong objects showing up in a layer could be due to cross-talk between the layers. However, we can see that for an increasing distance between layers, this greatly is reduced.

Overall, however, the reconstruction of the 3D structures shows promise, but for this simulated data reconstruction, some remarks have to be made. First, no Poisson noise was added. It would be interesting to add and then see how well the layers will be reconstructed. Furthermore, a flat probe was used, whereas in experiments often a speckle probe is preferred. In this simulation, a flat probe was chosen due to the limited time available, while the simulated probe did not result in trustworthy reconstructions. Therefore, for the further numerical study of the multilayer reconstruction, a speckle probe could be attempted to be used. Additionally, only two 2D layers were now used. However, in theory, as many layers could be simulated as allowed by the computational memory. Thus, it would be interesting to see how well the correlation remains in a variety of layers.

By this, a numerical simulation of a 3D object consisting of two independent 2D layers has shown that the Ptychoflow is able to reconstruct a 3D object to a high degree, even if the distance between the layers was only 10 μm .

5 Conclusion

In this work, I have illustrated a method to engrave any 2 or 3D object with equidistant laser damage sites. With that, I have been able to create 3D phase objects in BK-7 glass with high control over the objects, which could be useful for advancing any 3D phase imaging method. It would be interesting to utilise a different material than BK-7 glass. In theory, any material which is transparent and stable enough to endure laser engraving. An interesting idea would be to use ceramic glass as it shares the properties of glass allowing laser engraving, but the strength from ceramics. By using a 3D object created through sub-surface laser engraving, I have been able to extend and test the reconstruction of a 3D object through automatic differentiation ptychography. By using numerical data of a phase-only object, the reconstruction of 3D objects for a distance of the order of 10^2 μm , shows strong cross-talk between layers, resulting in similar layers resembling both layers. The cross-talk decreases with an increasing distance between layers, leading to better-reconstructed layers. Even without using any amplitude information in the numerical data, the algorithm is able to reconstruct the layers to a small degree. However, in the numerical data, no noise has been added, which in practice will reduce the reconstruction quality. Nevertheless, it is expected that the quality of the reconstruction will remain high. A potential use for the simulation would be to introduce the noise and inspect the influence. For further numerical testing, by adding layers to the 3D object, the limit for the number of layers to be reconstructed can be tested. Experimentally, the reconstruction of a phase object shows the phase and amplitude of the created 3D object in 2D. For an NA of 0.03 with a propagation distance of 6.2 cm, a resolution of 22 μm could be reached. By moving the camera to a propagation distance of 10 cm, the resolution of the reconstructed 3D object is improved to 10 μm . However, the reconstruction keeps showing a 3D object in 2D, as the reconstruction to show them in 3D, did not result in two layers of the 3D object. A reason could be the laser-engraved structures being too small to be noticed compared to chrome dots on the same side. However, a limitation of using a laser to create 3D objects is the time it takes for the engraving of large structures, assuming the glass will be able to endure the engraving. For a potential successor, an interesting experiment would be to place two chrome dots on opposites of a glass slide and attempt to reconstruct the layers. By performing this experiment, the limitations of sub-surface laser engraving would be removed, but the reconstruction in 3D should be more reasonable. Then, if the two chrome dots illustrate the algorithm is able to reconstruct the two layers through experimental data, more complex objects could be used. For example, a 3D object with three layers compared to two layers could be used. A potential application for 3D reconstruction without the need for lenses could be in the X-ray regime, where lenses are either expensive or not available. However, I can at the moment not guarantee a complex object would be able to be reconstructed to a high degree. However, with more testing and research I have faith that automatic differentiation ptychography can be used to reconstruct complex 3D objects in a range of regimes, from X-ray to visible light.

References

- [1] A. P. Sarvazyan, A. R. Skovoroda, S. Y. Emelianov, J. B. Fowlkes, J. G. Pipe, R. S. Adler, R. B. Buxton, and P. L. Carson, “Biophysical bases of elasticity imaging”, in *Acoustical imaging*, edited by J. P. Jones (Springer US, Boston, MA, 1995), pp. 223–240.
- [2] A. Iudin, P. K. Korir, S. Somasundharam, S. Weyand, C. Cattavittello, N. Fonseca, O. Salih, G. J. Kleywegt, and A. Patwardhan, “EMPIAR: the Electron Microscopy Public Image Archive”, *Nucleic Acids Research* **51**, D1503–D1511 (2022).
- [3] A. H. Jacobs, L. W. Kracht, A. Gossmann, M. A. Rüger, A. V. Thomas, A. Thiel, and K. Herholz, “Imaging in neurooncology”, *NeuroRX* **2**, Neuroimaging: Anything to Do with Neurotherapeutics?, 333–347 (2005).
- [4] J. P. Hornak, “Encyclopedia of imaging science and technology”, in (2002).
- [5] J. N. Mait, G. W. Euliss, and R. A. Athale, “Computational imaging”, *Adv. Opt. Photon.* **10**, 409–483 (2018).
- [6] R. Hegerl and W. Hoppe, “Beugung im inhomogenen prim irstrahlwellenfeld. i. prinzip einer phasenmessung von elektronenbeugungsinterferenzen”, *Berichte der Bunsengesellschaft für physikalische chemie* **74**, 1148–1154 (1970).
- [7] H. M. L. Faulkner and J. M. Rodenburg, “Movable aperture lensless transmission microscopy: a novel phase retrieval algorithm”, *Phys. Rev. Lett.* **93**, 023903 (2004).
- [8] M. Carlsen, T. M. RÄlder, C. Yildirim, R. Rodriguez-Lamas, C. Detlefs, and H. Simons, “Fourier ptychographic dark field x-ray microscopy”, *en, Opt Express* **30**, 2949–2962 (2022).
- [9] M. D. Seaberg, B. Zhang, D. F. Gardner, E. R. Shanblatt, M. M. Murnane, H. C. Kapteyn, and D. E. Adams, “Tabletop nanometer extreme ultraviolet imaging in an extended reflection mode using coherent fresnel ptychography”, *Optica* **1**, 39–44 (2014).
- [10] Y. Jiang, Z. Chen, Y. Han, P. Deb, H. Gao, S. Xie, P. Purohit, M. W. Tate, J. Park, S. M. Gruner, V. Elser, and D. A. Muller, “Electron ptychography of 2d materials to deep sub-angstrom resolution”, *Nature* **559**, 343–349 (2018).
- [11] S. Ghosh, Y. S. G. Nashed, O. Cossairt, and A. Katsaggelos, “Adp: automatic differentiation ptychography”, in 2018 IEEE International Conference on Computational Photography (ICCP) (2018), pp. 1–10.
- [12] Y. S. Nashed, T. Peterka, J. Deng, and C. Jacobsen, “Distributed automatic differentiation for ptychography”, *Procedia Computer Science* **108**, International Conference on Computational Science, ICCS 2017, 12–14 June 2017, Zurich, Switzerland, 404–414 (2017).
- [13] S. Kandel, S. Maddali, M. Allain, S. O. Hruszkewycz, C. Jacobsen, and Y. S. G. Nashed, “Using automatic differentiation as a general framework for ptychographic reconstruction”, *Opt. Express* **27**, 18653–18672 (2019).
- [14] J. Rodenburg and A. Maiden, “Ptychography”, in *Springer handbook of microscopy*, edited by P. W. Hawkes and J. C. H. Spence (Springer International Publishing, Cham, 2019), pp. 819–904.

- [15] K. Huff, *R&I industry scrapbook part5: early laser engraving*, (2004) <https://www.engraversjournal.com/legacyarticles/2244/> (visited on 01/15/2023).
- [16] I. Troitski, “Method and laser system for creating high-resolution laser-induced damage images”, *SPIE* **4579**, 392–399 (2001).
- [17] I. Troitski, “Laser-induced image technology”, *SPIE* **5664**, 293–301 (2005).
- [18] “Durability of the refractive index change induced by a single femtosecond laser pulse in glass”, *Optical Materials: X* **1**, 1–4 (2019).
- [19] A. Butkutė and L. Jonušauskas, “3d manufacturing of glass microstructures using femtosecond laser”, *Micromachines* **12**, 10.3390/mi12050499 (2021).
- [20] T. Brabec and F. Krausz, “Intense few-cycle laser fields: frontiers of nonlinear optics”, *Rev. Mod. Phys.* **72**, 545–591 (2000).
- [21] C. B. Schaffer, A. Brodeur, and E. Mazur, “Laser-induced breakdown and damage in bulk transparent materials induced by tightly focused femtosecond laser pulses”, *Measurement Science and Technology* **12**, 1784 (2001).
- [22] M. R. R. Vaziri, “Z-scan theory for nonlocal nonlinear media with simultaneous nonlinear refraction and nonlinear absorption”, *Appl. Opt.* **52**, 4843–4848 (2013).
- [23] S. L. Chin, T. -. Wang, C. Marceau, J. Wu, J. S. Liu, O. Kosareva, N. Panov, Y. P. Chen, J. -. Daigle, A. A. S. Yuan, W. W. Liu, T. Seideman, H. P. Zeng, M. Richardson, and R. L. Z. Z. Xu, “Advances in intense femtosecond laser filamentation in air”, *Laser Physics* **22**, 1–53 (2012).
- [24] I. Troitski and H. Henderson, “Method and laser system for production of high quality laser-induced damage images by using material processin made before and after image creation”, *SPIE* **4579**, 392–399 (2004).
- [25] O. Bunk, M. Dierolf, S. Kynde, I. Johnson, O. Marti, and F. Pfeiffer, “Influence of the overlap parameter on the convergence of the ptychographical iterative engine”, *Ultramicroscopy* **108**, 481–487 (2008).
- [26] J. Seifert, D. Bouchet, L. Loetgering, and A. P. Mosk, “Efficient and flexible approach to ptychography using an optimization framework based on automatic differentiation”, *OSA Continuum* **4**, 121–128 (2021).
- [27] A. M. Maiden and J. M. Rodenburg, “An improved ptychographical phase retrieval algorithm for diffractive imaging”, *Ultramicroscopy* **109**, 1256–1262 (2009).
- [28] K. A. M. Maathuis, J. Seifert, and A. P. Mosk, *Sensor fusion in ptychography*, 2022.
- [29] P. J. Bickel and K. A. Doksum, *Mathematical statistics : basic ideas and selected topics* (CRC Press, Boca Raton).
- [30] J. W. Goodman, “Introduction to fourier optics”, *Introduction to Fourier optics*, 3rd ed., by JW Goodman. Englewood, CO: Roberts & Co. Publishers, 2005 **1** (2005).
- [31] A. M. Maiden, M. J. Humphry, and J. M. Rodenburg, “Ptychographic transmission microscopy in three dimensions using a multi-slice approach”, *J. Opt. Soc. Am. A* **29**, 1606–1614 (2012).
- [32] L. Loetgering, M. Du, K. S. E. Eikema, and S. Witte, “Zpie: an autofocusing algorithm for ptychography”, *Optics letters* **45**, 2030–2033 (2020).

- [33] T. M. Godden, R. Suman, M. J. Humphry, J. M. Rodenburg, and A. M. Maiden, “Ptychographic microscope for three-dimensional imaging”, *Opt. Express* **22**, 12513–12523 (2014).
- [34] A. Suzuki, S. Furutaku, K. Shimomura, K. Yamauchi, Y. Kohmura, T. Ishikawa, and Y. Takahashi, “High-resolution multislice x-ray ptychography of extended thick objects”, *Phys. Rev. Lett.* **112**, 053903 (2014).
- [35] Z. Xing, Z. Xu, X. Zhang, B. Chen, Z. Guo, J. Wang, Y. Wang, and R. Tai, “Virtual depth-scan multi-slice ptychography for improved three-dimensional imaging”, *Opt. Express* **29**, 16214–16227 (2021).
- [36] M. Vreugdenhil and D. van Oosten, “A highly automated apparatus for ultra-fast laser ablation studies”, *Review of Scientific Instruments* **93**, 073003 (2022).
- [37] C. A. Schneider, W. S. Rasband, and K. Eliceiri, “Nih image to imagej: 25 years of image analysis”, *Nature Methods*, 671–675 (2012).
- [38] D. Kingma and J. Ba, “Adam: a method for stochastic optimization”, *International Conference on Learning Representations* (2014).
- [39] J. Schindelin, I. Arganda-Carreras, E. Frise, V. Kaynig, M. Longair, T. Pietzsch, S. Preibisch, C. Rueden, S. Saalfeld, B. Schmid, J.-Y. Tinevez, D. J. White, V. Hartenstein, K. Eliceiri, P. Tomancak, and A. Cardona, “Fiji: an open-source platform for biological-image analysis”, *Nature Methods* **9**, 676–682 (2012).
- [40] X. Huang, H. Yan, R. Harder, Y. Hwu, I. K. Robinson, and Y. S. Chu, “Optimization of overlap uniformness for ptychography”, *Opt. Express* **22**, 12634–12644 (2014).
- [41] H. Vogel, “A better way to construct the sunflower head”, *Mathematical Biosciences* **44**, 179–189 (1979).
- [42] P. Virtanen, R. Gommers, T. E. Oliphant, M. Haberland, T. Reddy, D. Cournapeau, E. Burovski, P. Peterson, W. Weckesser, J. Bright, S. J. van der Walt, M. Brett, J. Wilson, K. J. Millman, N. Mayorov, A. R. J. Nelson, E. Jones, R. Kern, E. Larson, C. J. Carey, Í. Polat, Y. Feng, E. W. Moore, J. VanderPlas, D. Laxalde, J. Perktold, R. Cimrman, I. Henriksen, E. A. Quintero, C. R. Harris, A. M. Archibald, A. H. Ribeiro, F. Pedregosa, P. van Mulbregt, and SciPy 1.0 Contributors, “SciPy 1.0: Fundamental Algorithms for Scientific Computing in Python”, *Nature Methods* **17**, 261–272 (2020).
- [43] A. Torrisi, P. Wachulak, A. Bartnik, D. Adjei, J. Kostecki, L. Wegrzynski, R. Jarocki, M. Szczurek, and H. Fiedorowicz, “Desktop water window microscope using a double-stream gas puff target source”, *Applied Physics B* **118**, 10.1007/s00340-015-6044-x (2015).

A Creating numerical data

To reconstruct both experimental data and numerical data, a parameter file is required. In the case of experimental data, the following file was used:

```
sample_info:{'amplitude_type': 'uniform', 'phase_type': 'uniform',
'amplitude_range': (0, 1), 'phase_range': (0, 1)}

prop_method: 'as'
shift_method: 'ft_shift'
precision: 'float32'
num_mode_probe: 1
background_removal: True

# Optimization parameters

scan_pos_centering: True
randomize_order: True
optimizer_type: 'Adam'
scheduler_type: 'ExponentialDecay'

#decay_rate:{'scan_pos': [0.99], 'sample': [0.99], 'probe': [0.99],
'wavlen': [0.99], 'prop_dist': [0.99],
'background': [0.99], 'scan_fac': [0.99]}

cmap:('turbo', 'twilight')

probe_info:{'size': [(1500, 1500)], 'center': [(0, 0)], 'angle': [0],
'type': ['aperture']}
```

In the case of simulated data, the following file is used:

```
precision: 'float32'
wavlen: [0.561]
weights_wavlen: [1]
dispersive_sample: False
camera_pixel_num: 1024
num_mode_sample: 1
num_mode_probe: 1
noise_level: 0
shift_method: 'pixelated_shift'
prop_method: 'as'
camera_resizing_factor: 1
saturation: 0

sample_type: ['slice']

# multi-slice options
sample_num: 2
```

```
nb_list:[1.52]

n0:1.0

# sample init
#sample_type: 'uniform'

# Optimization parameters
weights_mode_sample:[1]
weights_mode_probe:[1]
scan_pos_centering:True
epoch_size:[2]
batch_size:[1]
batch_size_list:[1]
learn_rate_list:[0.1]

learn_rate:{'sample': [0.1], 'probe': [0.0], 'background': [0],
'wavlen': [0], 'scan_pos': [0],
'prop_dist': [0.0], 'scan_fac': [0.0]}

randomize_order:True
background_removal:False
optimizer_type:'Adam'
scheduler_type:'ExponentialDecay'
decay_rate:{'scan_pos': [0.99], 'sample': [0.99],
'probe': [0.99], 'wavlen': [0.99], 'prop_dist': [0.99],
'background': [0.99]}
cmap:('turbo', 'twilight')
sample_info:{'amplitude_type': 'uniform',
'phase_type': 'uniform', 'amplitude_range': (0, 1), 'phase_range': (0, 1)}

probe_info:{'size': [(1500, 1500)], 'center': [(0, 00)],
'angle': [0], 'type': ['aperture']}

dz_list:[0000000000.0]
```

To create numerical data, the following script is used:

```
# -*- coding: utf-8 -*-

"""
Created on Tue Aug 30 16:32:10 2022

@author: Dennis
"""
```

```
### Handlings paths
import os

our_path = os.getcwd()

# Add local_path.txt and type in the path to PtychoFlow in one line
with open('local_path.txt', 'r') as file:
    ptycho_path = file.read().rstrip()

### Imports

# Switch to PtychoFlow directory
os.chdir(ptycho_path)
print(os.chdir(ptycho_path))

# !git checkout multislice
#
import tensorflow as tf
from CoreTF import Models
from Core import Files
from Core.Ptychography import Ptychography
from Core.Visualization import viz
import numpy as np
import h5py
import matplotlib.pyplot as plt
import matplotlib
from PIL import Image
from scipy.ndimage import gaussian_filter
from pathlib import Path
from skimage.transform import rescale
from Core import UtilitiesNP
import h5py

def rescale_image(img, min_value=0.2, max_value=1.):
    img -= np.min(img)
    img /= np.max(img) # (0, 1)
    img *= max_value - min_value
    img += min_value
    return img

### Load and prepare images and sample

os.chdir(our_path)

size_array= np.empty([512,512])

lay1 = np.zeros_like(size_array)
lay1[:256,:] = 1
Array = np.zeros_like(size_array)
```

```
Array[:, :256] = 1
```

```
lay1 = np.pad(lay1, (512 - lay1.shape[0]) // 2)
Array = np.pad(Array, (512 - Array.shape[0]) // 2)
# sample = np.dstack((lay1, Array))
blur_value = 1.1
noise_value = 0.2
min_value = 0.2
```

```
camara_man_path = Path("./Images/cameraman.png")
camera_man = Image.open(camara_man_path).convert('L')
camera_man = np.array(camera_man).astype(np.float32)
camera_man = camera_man[5:485, 2:482]
camera_man = rescale_image(camera_man, min_value, 1)
# camera_man = np.random.poisson(camera_man * 255.0 * noise_value) / noise_value / 255
camera_man = np.pad(camera_man, (512 - camera_man.shape[0]) // 2)
camera_man = gaussian_filter(camera_man, blur_value)
```

```
mandril_path = Path("./Images/Mandril.png")
mandril = Image.open(mandril_path).convert('L')
mandril = np.array(mandril).astype(np.float32)
mandril = rescale(mandril, 480 / mandril.shape[0])
mandril = rescale_image(mandril, min_value, 1)
# mandril = np.random.poisson(mandril * 255.0 * noise_value) / noise_value / 255
mandril = np.pad(mandril, (512 - mandril.shape[0]) // 2)
mandril = gaussian_filter(mandril, blur_value)
```

```
# sample = sample1
# %% visualise them
# plt.figure()
# plt.imshow(lay1)
# plt.imshow(sample[:, :, 0])
# plt.colorbar()
# plt.title('Simulated Vertical grid')
# plt.xlabel('Pixels')
# plt.ylabel('Pixels')
```

```
# %% Generate scanning positions
```

```
def get_fermat_spiral(total_points, start_pos, radius, return_ind=0):
    """ Returns 2D scanning coordinates with 'optimal uniformness' for
    ptychography. According to Huang et al. (2014), this might be
    a Fermat spiral.
    INPUTS:
        - total_points: total scanning points (result will be round-ish)
        - start_pos: offset for the spiral center
        - radius: max. "radius" of the spiral (in mm)
        - return_ind: returns a mask with for selecting ::return_ind
    """
    # import sys
```



```
# if np.min(start_pos) < radius:
#     print('WARNING: Inputs allow physical scanning positions < 0.')
#     print('Stopping script.')
#     sys.exit()

fermat_spiral = np.zeros((2, total_points))

# Fermat spiral definition:
n = np.linspace(1, total_points, total_points)
c = radius / np.sqrt(total_points)
r = c * np.sqrt(n)
theta_0 = np.deg2rad(137.505)
theta = n * theta_0

# Converting to cartesian coordinates:
fermat_spiral[0, :] = r * np.cos(theta)
fermat_spiral[1, :] = r * np.sin(theta)

return 1e3* np.swapaxes(fermat_spiral, 0, 1)

# scan_points = get_fermat_spiral(150, 0, 3.52)
scan_points = np.zeros((1,2))
#%% Plot scanning points

# plt.figure()
# plt.scatter(scan_points[:, 0], scan_points[:, 1])
# plt.title("Number of scanning points: " + \
#           str(scan_points.shape[0]))
# plt.show()

#%% Generate probe, either speckle or flat
pixel_num = (1024, 1024)
pixel_size = (6.9, 6.9)
probe_sampling = (pixel_num, pixel_size)

def gen_gaussian(sampling, center, size, angle, wavlen=0, defocus=0):
    (yy, xx) = UtilitiesNP.gen_coordinates(sampling)
    (ly, lx) = size # diameter

    if defocus == 0:
        # beam field
        uy = np.exp(-(yy / (ly / 2)) ** 2)
        ux = np.exp(-(xx / (lx / 2)) ** 2)

    else:
        # rayleigh_range
        zry = np.pi * (ly / 2) ** 2 / wavlen
        zrx = np.pi * (lx / 2) ** 2 / wavlen
```

```
# beam parameter
qzy = defocus + 1j * zry
qzx = defocus + 1j * zrx
# beam field
uy = qzy ** (-1 / 2) * np.exp(-1j * (2 * np.pi / wavlen) * yy ** 16 / 2 * q
ux = qzx ** (-1 / 2) * np.exp(-1j * (2 * np.pi / wavlen) * xx ** 16 / 2 * q

# generate probe
probe = uy * ux

return probe

def gen_speckle(dim=1024, radius=0.5):

    random_phase = np.random.uniform(0, 2*np.pi, size=(dim, dim))

    xx, yy = np.meshgrid(np.linspace(-1, 1, dim),
                        np.linspace(-1, 1, dim))

    aperture = np.where(xx**2 + yy**2 > radius**2, 0, 1)

    speckle_F = aperture * np.exp(1j*random_phase) # Fourier domain

    speckle = np.fft.fft2(np.fft.fftshift(speckle_F))

    return speckle

probe = np.reshape(gen_gaussian(probe_sampling, (0, 0), (2800, 2800), 0), (1,1,1024

# probe = np.load(Path("./data/Optimized_probe.npy"))
probe_abs = np.abs(probe)
probe_abs[probe_abs < 0.8] = 0
probe_abs = gaussian_filter(probe_abs, 5)

# Assign phase to sample and probe

r = np.pi
x = np.linspace(-r, r, 1024)
xx, yy = np.meshgrid(x, x)
probe_phase = xx**2 + yy**2

flat_probe = 5e1 * probe_abs * np.exp(1j*(probe_phase))
```

```
# Speckle probe
# speckle_probe = gen_speckle(radius=0.05) * probe_abs[0,0,:,:)

# viz(speckle_probe)

# viz(flat_probe[0,0,:,:])
#
# speckle_probe = speckle_probe[np.newaxis, np.newaxis, ...]

#%% Building Ptychography model

params_path = "params_run.txt"
ptychogram_path = "./synthetic_data/ptychogram.npz"

main = Ptychography(params_path, ptychogram_path)
main.load_params()
# main.params.params['sample_type'] = [['2d']]
#main.params.params['wavlen'] = [100.0]

#%%
main.print_params()
main.check_params()

main.ptychogram.scan_pos = scan_points
main.ptychogram.scan_fac = np.ones((scan_points.shape[0], 1))
main.calcu_sampling()
main.print_sampling()

# main.probe = speckle_probe
main.probe = flat_probe
# viz(main.probe)
#%% assemble the object

num_pixel_object = 869
scaling_factor = num_pixel_object / lay1.shape[0]
sim_sample = np.zeros((2, 1, 1, main.sample_sampling[0][0],
                      main.sample_sampling[0][1]), dtype=np.complex64)

layer1 = rescale(lay1, scaling_factor)
x_pad = (main.sample_sampling[0][0] - num_pixel_object) // 2
y_pad = (main.sample_sampling[0][1] - num_pixel_object) // 2
layer1 = np.pad(layer1, ((x_pad, x_pad), (y_pad, y_pad)))

Array = rescale(Array, scaling_factor)
layer2 = np.pad(Array, ((x_pad, x_pad), (y_pad, y_pad)))

#
sim_sample[0, 0, 0, :, :] = layer1
```

```
sim_sample[1, 0, 0, :, :] = layer2

main.sample = sim_sample

# np.save('Camera_ground_truth_fixed', layer1)
# np.save('Mandrill_ground_truth_fixed', layer2)

#%% visualise sample
viz(main.sample[0,0,0,:,:])
viz(main.sample[1,0,0,:,:])

#%% build model and run simulation

mask = np.ones((1024, 1024))
main.ptychogram.mask = mask
background = np.zeros((1024, 1024))
main.ptychogram.background = background
with tf.device('/job:localhost/replica:0/task:0/device:GPU:0'):
    main.build_model()

# main.dashboard()

#%% simulate diffraction patterns

diff_pat_list = []
num_patterns = len(main.ptychogram.scan_pos)
for i in range(num_patterns):
    a = main.model(tf.constant([i]))
    diff_pat_list.append(a.numpy().reshape((1024, 1024)))
diff_pat_list = np.array(diff_pat_list)

main.ptychogram.diff_pat = diff_pat_list
#%% show some diffraction patterns

# plt.figure(figsize=(10, 10))

# plot_indices = np.linspace(0, num_patterns - 1, 9, dtype=int)

# for k in range(9):
#     plt.subplot(3, 3, k+1)
#     plt.imshow((diff_pat_list[plot_indices[k], :, :]))
#     plt.colorbar()
#     plt.axis('off')

# plt.show()
viz(main.ptychogram.diff_pat[0,:,:])
```

```
### functions to save Ptychogram as HDF5 or npz for an initially empty file
```

```
def save_simulation_data_hdf5(file_name, diff_pat_list, scan_points,
                             background, mask, datatype):
```

```
    save_path = '{}.hdf5'.format(file_name)
    with h5py.File(save_path, 'w') as f:
        f.create_dataset('diff_pat', data=diff_pat_list,
                        dtype=datatype)
        f.create_dataset('scan_pos', data=scan_points,
                        dtype=datatype)
        f.create_dataset('background', data=background,
                        dtype=datatype)
        f.create_dataset('mask', data=mask,
                        dtype=datatype)
```

```
### Saving simulated diffraction patterns
```

```
file_name = Path('./data/simulated_ptychogram_3D')
datatype = 'float32'
save_simulation_data_hdf5(file_name, diff_pat_list, scan_points,
                          background, mask, datatype)
print('File saved as hdf5')
```

```
# %% save probe ground truth
```

```
# np.savez_compressed('./probe_ground_truth.npz', main.probe)
#
```

To reconstruct the numerical data, the following script was used:

```
# -*- coding: utf-8 -*-
"""
```

```
Created on Fri Sep 9 11:39:37 2022
```

```
@author: Dennis
"""
```

```
### Handlings paths
import os
```

```
our_path = os.getcwd()
```

```
# Add local_path.txt and type in the path to PtychoFlow in one line
with open('local_path.txt', 'r') as file:
    ptycho_path = file.read().rstrip()
```

```
### Imports
```

```
# Switch to PtychoFlow directory
```

```
os.chdir(ptycho_path)

# !git checkout multislice

import tensorflow as tf
from CoreTF import Models
from Core import Files
from Core.Ptychography import Ptychography
from Core.Visualization import viz
import numpy as np
import h5py
import matplotlib.pyplot as plt
import matplotlib
from PIL import Image
from scipy.ndimage import gaussian_filter
from pathlib import Path

#%% Load ptychogram
os.chdir(our_path)

params_path = "params_run.txt"

ptychogram_path = Path('./data/simulated_ptychogram_3D.hdf5')
main = Ptychography(params_path, ptychogram_path)
main.load_params()

# %% load probe ground truth
probe_gt = np.load('probe_ground_truth.npz')['arr_0']
# viz(probe_gt)
#
#%% Alter parameters if needed

main.params.params['epoch_size'] = [70]
main.params.params['learn_rate']['sample'] = [0.01] # play with
main.params.params['learn_rate']['probe'] = [0.00] # play with

#%% Initialise functions

main.load_ptychogram()
main.check_params()
# main.params.params['probe_info']['size'] = [(2000, 2000)]
main.print_params()

main.center_scan_pos()
main.remove_background()
main.resize_camera()
```

```
main.print_ptychogram()
main.calcu_sampling()
main.print_sampling()
main.init_sample()
main.init_probe()

main.probe = probe_gt

#%% Build model and optimize
# probe = np.load(Path("./data/Optimized_probe.npy"))
# main.probe = probe
with tf.device('/job:localhost/replica:0/task:0/device:GPU:0'):
    main.build_model()
    main.params.params["regularizer"]['sample_l1'] = [0.1] # play with
    main.optimize()

#%% Save simulation

#main.save_results()
# main.save_result()
main.update_main()
# main.save_result()
# np.save(main.sample, 'test_save_sample_dz_{main.params.params[dz_list]}_mictrometr
dz = main.params.params['dz_list']
# sample = f'./results/test_save_sample_dz_mictrometre_{a}'
# np.save(sample, main.sample)

# main.clear_history()

output_folder = './Fixed_probe_run2/'

np.savez_compressed(output_folder+str(dz)+'.npz',
                    sample=main.sample,
                    dz=dz)
```